Monthly Notices of the ROYAL ASTRONOMICAL SOCIETY

MNRAS **532,** 1564–1579 (2024)
Advance Access publication 2024 July 4

https://doi.org/10.1093/mnras/stae1571

XMM–Newton Ultra Narrow Deep Field survey – II. X-ray spectral analysis of the brightest AGN population

M. Elías-Chávez [1★], A. L. Longinotti [2], Y. Krongold [2], D. Rosa-González [3], C. Vignali [4,5], S. Mathur [6,7], T. Miyaji [1], Y. D. Mayya[3] and F. Nicastro[8,9]

[1]*Instituto de Astronomía, Universidad Nacional Autónoma de México., Apdo. Postal 106, 22800 Ensenada, B.C., México*
[2]*Universidad Nacional Autónoma de México, Instituto de Astronomía, Apdo. Postal 70-264, I-04510. Ciudad de México, México*
[3]*Instituto Nacional de Astrofísica, Óptica y Electrónica, Luis E. Erro 1, Tonantzintla, Puebla, Apdo. Postal 72840, Mexico*
[4]*Dipartimento di Fisica e Astronomia, Università di Bologna, viale Berti Pichat 6/2, I-40127 Bologna, Italy*
[5]*INAF - Osservatorio di Astrofisica e Scienza dello Spazio di Bologna, Via Gobetti 93/3, I-40129 Bologna, Italy*
[6]*Department of Astronomy, The Ohio State University, 140 West 18th Avenue, Columbus, OH 43210, USA*
[7]*Center for Cosmology and Astroparticle Physics, 191 West Woodruff Avenue, Columbus, OH 43210, USA*
[8]*Osservatorio Astronomico di Roma-INAF, Via di Frascati 33, I-00040 Monte Porzio Catone, RM, Italy*
[9]*Department of Astronomy, Xiamen University, Xiamen, Fujian 361005, China*

Accepted 2024 June 21. Received 2024 June 12; in original form 2023 December 15

ABSTRACT

In this work, we present the results of a detailed X-ray spectral analysis of the brightest active galactic nuclei (AGNs) detected in the *XMM–Newton* 1.75 Ms Ultra Narrow Deep Field. We analysed 23 AGNs that have a luminosity range of $\sim 10^{42}$–10^{46} erg s^{-1} in the 2–10 keV energy band, redshifts up to 2.66, and $\sim$ 10 000 X-ray photon counts in the 0.3–10 keV energy band. Our analysis confirms the 'Iwasawa–Taniguchi effect,' an anticorrelation between the X-ray luminosity (L_x) and the Fe–kα equivalent width ($\mathrm{EW_{Fe}}$) possibly associated with the decreasing of the torus covering factor as the AGN luminosity increases. We investigated the relationship among black hole mass (M_{BH}), L_x, and X-ray variability, quantified by the Normalized Excess Variance (σ^2_{rms}). Our analysis suggest an anticorrelation in both $M_{\mathrm{BH}} - \sigma^2_{\mathrm{rms}}$ and $L_x - \sigma^2_{\mathrm{rms}}$ relations. The first is described as $\sigma^2_{\mathrm{rms}} \propto M_{\mathrm{BH}}^{-0.26\pm0.05}$, while the second presents a similar trend with $\sigma^2_{\mathrm{rms}} \propto L_x^{-0.31\pm0.04}$. These results support the idea that the luminosity–variability anticorrelation is a byproduct of an intrinsic relationship between the BH mass and the X-ray variability, through the size of the emitting region. Finally, we found a strong correlation among the Eddington ratio (λ_{Edd}), the hard X-ray photon index (Γ), and the illumination factor $\log(A)$, which is related to the ratio between the number of Compton scattered photons and the number of seed photons. The $\log(\lambda_{\mathrm{Edd}}) - \Gamma - \log(A)$ plane could arise naturally from the connection between the accretion flow and the hot corona.

Key words: surveys – galaxies: active – quasars: supermassive black holes – X-rays: galaxies.

1 INTRODUCTION

Active galactic nuclei (AGNs) are among the most luminous objects in the Universe. They reside in galaxies that harbour a Super Massive Black Hole (SMBH) at their centres, with a mass range of $M_{\mathrm{BH}} \sim 10^{5-10}\,\mathrm{M}_{\odot}$, powered by an accreting disc of gas (Kormendy & Richstone 1995). The huge amount of energy generated in their nuclear region can reach X-ray luminosities higher than 10^{46} erg s^{-1} with bolometric luminosities $L_{\mathrm{bol}} \approx 10^{42-48}$ erg s^{-1} (Hickox & Alexander 2018). The X-ray radiation observed in AGNs is thought to be produced primarily by the process of comptonization. In this process, optical/UV disc photons are scattered by a corona of hot electrons located above the accretion disc (George & Fabian 1991; Haardt & Maraschi 1991; Matt et al. 1997).

X-ray surveys conducted by satellites such as *XMM–Newton*, *Chandra*, and more recently *eROSITA* serve as highly effective methods for AGN identification (e.g. Luo et al. 2017; Chen et al. 2018; Liu et al. 2022). For instance, X-ray emission resulting from the accretion process on to SMBHs can penetrate through high hydrogen column densities ($N_H \approx 10^{21}$–$10^{24.5}$ cm^{-2}), and experience minimal dilution by starlight from the host galaxy (Brandt & Alexander 2015). As a result, X-ray surveys allow to census large samples of both obscured ($N_{\mathrm{H}} \geq 10^{22}$ cm^{-2}) and unobscured ($N_{\mathrm{H}} < 10^{22}$ cm^{-2}) AGNs and their host galaxies across different redshift ranges (Hickox & Alexander 2018). This feature facilitates studies such as the connection between SMBHs and galaxy formation, the contribution of these sources to the Cosmic X-ray Background (XRB; Gilli, Comastri & Hasinger 2007), and to test models of quasar formation and AGN evolution (Scoville et al. 2007; Kellermann et al. 2008; Rosen et al. 2016; Brandt & Vito 2017).

X-ray spectral analysis is a powerful diagnostic tool to investigate the physical properties of AGNs. It enables the estimation of

★ E-mail: melias@astro.unam.mx

© 2024 The Author(s).
Published by Oxford University Press on behalf of Royal Astronomical Society. This is an Open Access article distributed under the terms of the Creative Commons Attribution License (https://creativecommons.org/licenses/by/4.0/), which permits unrestricted reuse, distribution, and reproduction in any medium, provided the original work is properly cited.

Downloaded from https://academic.oup.com/mnras/article/532/2/1564/7706312 by Instituto Nac. de Astrofisica, optica y Electronica (INAOE) user on 11 July 2024

parameters such as intrinsic absorption $N_{\rm H}$, black hole mass $M_{\rm BH}$, X-ray luminosity L_x, and to characterize the nuclear region surrounding the SMBH (Brandt & Vito 2017). One of the main spectral features commonly observed in most AGNs is the Fe−Kα emission line at 6.4 keV, which is generated as a consequence of the X-ray fluorescence process. The analysis of the Fe−Kα is fundamental to studying the structure of the torus and inner regions of AGNs, such as the accretion disc properties (Fragile, Miller & Vandernoot 2005). For instance, Iwasawa & Taniguchi (1993) and Bianchi et al. (2007) have demonstrated the presence of an anticorrelation between the Fe−Kα equivalent width ($\rm EW_{Fe}$) and the X-ray luminosity in the 2–10 keV energy range. This relationship, described as $\rm EW_{Fe} \propto L_x^{-0.2}$, has been referred to as the 'Iwasawa-Taniguchi effect' or the 'X-Ray Baldwin Effect'. Some studies have proposed that it arises from the decreasing of the opening angle of the torus as a function of the increasing of the AGN luminosity (Bianchi et al. 2007; Ricci et al. 2014). Another possibility is the decreasing amount of low-ionization material available to generate the fluorescence Fe−K α line, due to the increase of the X-ray luminosity that ionizes the neutral iron in the torus (Shu, Yaqoob & Wang 2010). During our analysis, we will investigate the 'Iwasawa−Taniguchi effect' using a collection of new high-quality AGN spectra.

Most AGNs exhibit short-term and long-term X-ray variability, which is thought to be generated due to changes in the accretion flow (Yuan & Narayan 2014), instabilities in the disc corona (McHardy et al. 2004), or variable-density absorptions, among other factors influenced by the accretion dynamics and the surrounding environment (Beuchert et al. 2015). Taking advantage of this feature, certain X-ray studies have contributed with novel techniques to identify and characterize AGNs samples, infer their general properties, and investigate the contribution of $M_{\rm BH}$ to the variability–luminosity relation. For example, Nikolajuk, Papadakis & Czerny (2004) and Ponti et al. (2012) employed the normalized excess variance ($\sigma^2_{\rm rms}$), a parameter that quantifies the X-ray flux variation, to estimate the BH mass in local unobscured Radio-Quiet AGNs. Lanzuisi et al. (2014) analysed the long-term variability of the brightest AGNs detected in the XMM Cosmic Evolution Survey (XMM-COSMOS). They reported a significant anticorrelation between the X-ray luminosity and the X-ray flux variability, suggesting the possibility that the observed luminosity–variability relationship is a consequence of an intrinsic $M_{\rm BH}$–variability relation.

The accretion process in AGNs plays a crucial role in determining the cosmic evolution of SMBHs. A meaningful physical parameter that offers valuable insights into the BH growth is the Eddington ratio $\lambda_{\rm Edd} = L_{\rm bol}/L_{\rm Edd}$ (Trump et al. 2011; Georgakakis et al. 2017; Laurenti et al. 2022), which is defined as the ratio between the bolometric luminosity $L_{\rm bol} = \eta \dot{M}_{\rm BH} c^2$ where η describes the efficiency of the accretion process, and the Eddington luminosity $L_{\rm Edd}$. $L_{\rm bol}$ can be estimated from the X-ray luminosity (Netzer 2013). $L_{\rm Edd}$ represents the maximum luminosity allowed by a steady-state accretion, at which the radiation pressure balances the gravitational force. For instance, Trump et al. (2011) demonstrated the utility of accretion rate to distinguish between unobscured broad-line, narrow-line, and lineless AGNs, after analysing a sample of 153 AGNs. The research revealed that high accretion rates ($\lambda_{\rm Edd} > 0.01$) were predominantly associated with broad-line AGNs and some potentially obscured narrow-line AGNs. In contrast, narrow-line and lineless AGNs exhibited lower specific accretion rates ($\lambda_{\rm Edd} < 0.01$) and higher radio-to-optical/UV emission ratios. In the highest accretion regime, Laurenti et al. (2022) reported significant dispersions in key spectral parameters (e.g. $\Gamma = 1.3$–2.5) for a small group of highly accreting AGNs ($\lambda_{\rm Edd} > 1$), with approximately 30 per cent classified as X-ray weak quasars.

In this paper, we analysed the main X-ray spectral properties of the brightest AGNs detected in one of the deepest surveys observed by *XMM–Newton*. We searched for any relationship among the accretion process and the X-ray variability represented by $\lambda_{\rm Edd}$ and $\sigma^2_{\rm rms}$, respectively, and other physical parameters of our AGN sample, including X-ray luminosity, BH mass, $K\ \alpha$ iron emission line, photon index, and intrinsic column density. This paper is organized as follows: in Section 2, we provided a description of the AGN sample and the XMM–UNDF survey. We outlined the *XMM−Newton* observations, the available multiwavelength data, and the main properties of the AGNs. The X-ray spectral analysis, including the modeling and its results, is presented in Section 3. Section 4 focuses on the study of the primary spectral parameters. The X-ray variability, the BH mass estimations, and a linear regression Monte Carlo simulation are presented in Section 5. Then, in Section 6 we present an analysis of the accretion rate distribution of our AGNs and in Section 7 we summarize the key outcomes of our analysis.

Throughout this work, we adopted the cosmological parameters $H_0 = 70\,{\rm km\,s^{-1}\,Mpc^{-1}}$, $\Omega_{\rm m} = 0.3$, and $\Omega_\Lambda = 0.7$.

2 X-RAY SURVEY AND SAMPLE SELECTION

2.1 The XMM−UNDF survey

The *XMM−Newton* Ultra Narrow Deep Field survey, detailed in our previous study of Elías-Chávez et al. (2021, paper I hereafter) and renamed as XMM−UNDF, consists of 13 observations taken over 2 yr with a total exposure time of 1.75 million seconds (Ms) in a field of 900 arcmin^2 (Nicastro et al. 2018) around the high luminous blazar 1ES 1553 + 113 ($F_{0.3-10\,\rm keV} \approx 2 \times 10^{-11}\,{\rm erg\,s^{-1}\,cm^{-2}}$). With a flux limit of $4.03 \times 10^{-16}\,{\rm erg\,s^{-1}\,cm^{-2}}$ in the 0.2–2.0 keV energy band. The XMM–UNDF is the deepest survey observed by *XMM–Newton* centered around a bright source and the third with the highest sensitivity. It was complemented with deep optical broadband images with the *Sloan Digital Sky Survey* (SDSS) filters u', g', r', i', and z' obtained with the OSIRIS instrument mounted on the Gran Telescopio Canarias (GTC), down to magnitude $r \sim 24.5$. Additionally, this field presents IR coverage with *WISE* and 2MASS observatories in the Mid (W_1, W_2, W_3, and W_4) and Near (J, H, and K_s) infrared bands, respectively, with detections at signal-to-noise ratio (SNR) > 5 (Cutri et al. 2021). Fig. 1 presents the mosaic of X-ray images of the field with optical (GTC) and infrared (*WISE*) observational coverage. The cyan circles highlight the AGN sample of our analysis.

2.2 X-ray data products

The X-ray data processing was performed with the XMM−Newton Science Analysis Software version 18 (SAS; Gabriel et al. 2004). The tasks `epproc` and `emproc` provided by the EPICPROC package were utilized to prepare the observations and generate data products such as light curves, spectra, images from the EPIC instruments (PN, MOS1, MOS2 cameras). Afterwards, source detection was performed using the task `edetec_stack`, specifically developed for multiepoch *XMM–Newton* observations (Traulsen et al. 2019, 2020). For more details on the AGN identification process, X-ray source detection, and data reduction, refer to Paper-I.

Downloaded from https://academic.oup.com/mnras/article/532/2/1564/7706312 by Instituto Nac. de Astrofisica, optica y Electronica (INAOE) user on 11 July 2024

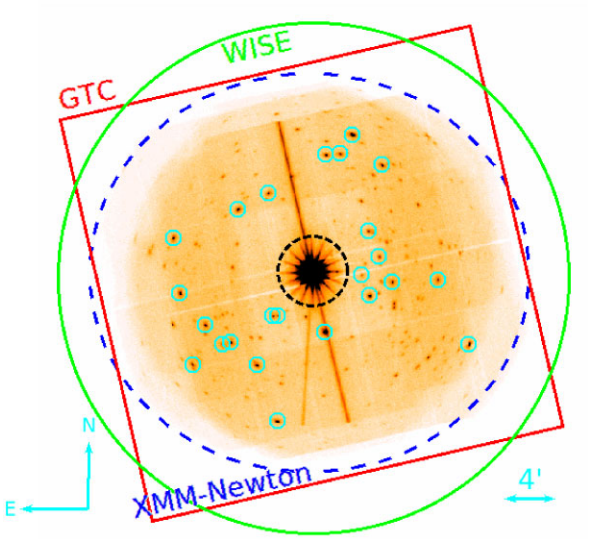

Figure 1. Mosaic image of the X-ray survey at 0.3–10 keV band. Our AGN sample is represented with cyan circles. The full optical GTC-Field is marked by a red square of 33 arcmin sides, the blue ellipse refers to the *XMM−UNDF* of about 30 arcmin × 30 arcmin, and the green circle of 20 arcmin radius is for the infrared *WISE* field.

2.3 The AGN sample

In Paper-I, we reported an X-ray-Optical-IR catalogue consisting of 301 sources detected at a significance level of 3σ in the XMM–UNDF survey.[1] The majority (244; 81 per cent) of the objects in the catalog possess at least one optical or infrared counterpart association. Among these sources, 204 were classified as AGNs based on criteria involving X-ray luminosity, X-ray/optical, and X-ray/IR flux ratios, as carried out in other X-ray surveys (Xue et al. 2011; Luo et al. 2017; Chen et al. 2018).

In the present analysis, we selected a subsample of the brightest AGNs that were detected with at least 500 photon counts (cts) on average per observation in the 0.3–10 keV energy band with the PN camera. For instance, a source detected in 11 observations will have at least 5500 cts in total with the PN camera to satisfy this criterion. This threshold ensured a sufficient level of statistical quality in each individual X-ray spectrum. As a result, we reduced the list to 23 AGNs that met this requirement with a median X-ray count of $\sim 10\,000$ cts and X-ray flux range from 3×10^{-13} to 2×10^{-14} erg s^{-1} cm^{-2} in the 0.3–10 keV band, all with optical and infrared counterparts, except for three sources for which we did not detect *WISE* infrared emission. The total and average photon count distributions of our AGN sample are presented in Fig. 2 with the black and red histograms, respectively. Table 1 reports their main multiwavelength properties.

3 X-RAY SPECTRAL ANALYSIS

3.1 Stacking multiple spectra

Given that the XMM–UNDF survey consists of multiple observations centred in the same field, we employed a spectral stacking approach to enhance the signal-to-noise ratio and minimize statistical uncertainties. We extracted and combined the individual spectra of each AGN from our sample using 11 out of 13 observations that were conducted in a PN full window mode, i.e. the 2 PN small window observations (0761100701 and 0790381001) were not considered in this analysis.[2] To combine the spectra, we followed the XMM-Newton data analysis thread 'Combining the spectra of the 3 epic cameras'.[3] We used the task `epicspeccombine` to merge the spectra of the three EPIC cameras (PN, MOS1, and MOS2) whenever they were available from the 11 observations. This resulted in a single spectrum with its corresponding calibration matrices (rmf, arf) and background (bkg) files. The procedure we followed is outlined below:

(i) We begin by using the task `evselect` to extract all source and background spectra from manually selected regions in the 3 cameras, we used circular areas of 15 and 30 arcsec, respectively. These regions correspond to about 75 per cent of the encircled energy fraction. An example is presented in Fig. 3 with the source XID-7.

(ii) Then, the `backscale` task was used to calculate the areas of the source and background regions.

(iii) For each extracted spectrum, the redistribution matrix file (rmf) and auxiliary response file (arf) were generated using the `rmfgen` and `arfgen` tasks.

(iv) To ensure adequate statistical quality and prevent oversampling of the energy resolution by more than a factor of 3, the `specgroup` task was used to rebin the spectrum and link the associated files to have at least 25 counts for each background-subtracted spectral channel.

(v) Finally, all individual spectra from the three cameras and the 11 observations were combined into one single spectrum using the `epicspeccombine` task.

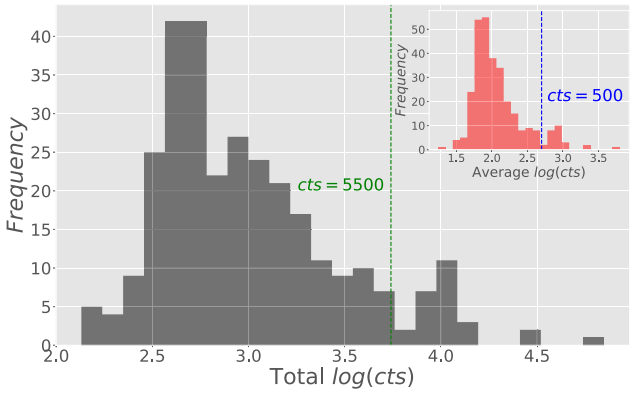

Figure 2. Histograms of the stacked observations (black) and average-per-observation (red) X-ray counts of our AGN population in the XMM–UNDF survey in the 0.3 − 10 keV band, the green and blue dotted lines limit the regions for those objects that were detected with 5500 counts in total and 500 in average-per-observation with the PN camera, respectively.

3.2 Spectral fitting and modelling

For our study, we used the software XSPEC version 12.10.0 to perform the X-ray spectral fitting. We employed a set of simple absorbed

[1]The full X-ray catalogue is available online at https://doi.org/10.26093/cds/vizier.19190018.

[2]In Paper I, the central region of the observations around the bright blazar (marked with the black circle in Fig. 1) was avoided during the source detection process. This region covers most of the small window field of view.

[3]https://www.cosmos.esa.int/web/xmm-newton/sas-thread-epic-merging

Downloaded from https://academic.oup.com/mnras/article/532/2/1564/7706312 by Instituto Nac. de Astrofisica, optica y Electronica (INAOE) user on 11 July 2024

Table 1. Multiwavelength parameters of our bright AGN sample detected in the XMM–UNDF survey. From *XMM–Newton* (cts, $F_{0.3-10\,\mathrm{keV}}$, and $L_{0.3-10\,\mathrm{keV}}$) and GTC ($u'g'r'i'$ and z') observations, and *WISE* (W_1, W_3, W_3, and W_4) public data. We maintained the same X-ray identification names (XID) from Paper-I.

XID	z	z_f [a]	cts	$F_{0.3-10\,\mathrm{keV}}$ 10^{-14} erg s^{-1} cm^{-2}	$L_{0.3-10\,\mathrm{keV}}$ 10^{44} erg s^{-1}	u' (mag)	g' (mag)	r' (mag)	i' (mag)	z' (mag)	W_1 (mag)	W_2 (mag)	W_3 (mag)	W_4 (mag)
1	2.66	s	70 046	30.44	260.77	20.2	19.4	19.3	19.3	19	16	15.2	11.5	8.42
2	0.134	s	27 437	14.38	0.007	20	18.8	18	17.5	17.1	14.9	14.7	12.2	9.09
3	0.757	s	9698	11.79	3.67	19.7	19.4	19.5	19.4	19	14.7	13.5	10.6	8.09
4	1.13	s	25 947	8.55	7.53	20.9	20.7	20.4	20.4	20.2	16.2	15.2	12.4	8.97
5	0.948	s	15 617	8.41	4.7	22.7	21.7	21.3	20.9	20.2	–	–	–	–
6	1.15	p	11 314	6.42	6.01	21.3	21.3	20.9	20.7	20.6	16.9	15.7	12.3	8.96
7	1.04	p	12 989	7.08	5.07	22.1	21.5	21.3	21.1	20.7	16	15	12	8.8
8	0.621	p	12 094	5.5	1.03	23.6	22.4	22.2	21.5	21.2	17.7	16.8	12.2	8.85
9	0.998	p	12 625	7.78	4.98	21.1	20.7	20.5	20.4	20.1	15.9	15.7	12.4	8.99
10	0.879	s	10 959	6.18	2.84	21.6	21.2	20.9	20.5	20.1	15.9	15.3	12	9.02
11	0.126	p	9640	4.92	0.002	20.1	19.7	19.5	19	19	16.4	15.2	12.1	8.64
12	0.749	p	10 243	4.97	1.51	21.9	21.3	21.3	20.8	20.9	18	16.2	12.1	8.25
13	0.842	p	10 105	4.81	1.97	22.6	22.5	21.9	21.7	21.3	16.8	15.6	12	9.05
14	1.43	s	9953	5.03	8.29	21.2	21	20.7	20.5	20.4	16.9	15.7	12	8.95
15	0.344	p	8393	5.97	0.26	22.4	21.4	20.6	20.2	19.9	16.2	14.9	11.4	8.5
16	0.386	p	9664	4.5	0.26	19.9	19.5	19.4	19.2	19.2	16.2	15.1	12.5	8.7
17	0.434	s	8901	3.27	0.25	23	22	20.5	19.8	19.3	15.9	15.5	12.7	9.09
18	0.61	p	7914	3.6	0.65	20.7	20.2	20.1	19.9	19.8	16.2	15	11.9	8.8
19	0.427	p	8749	4.31	0.32	23.2	22.1	21.8	21.3	21	16.6	15.4	11.9	8.55
20	0.589	p	10 418	4.21	0.69	23.8	23	22.7	22.1	22	–	–	–	–
8	0.722	s	9164	3.35	0.92	22.7	22	21.6	20.8	20.4	16.1	15.7	12.2	8.66
33	0.458	p	6265	2.05	0.18	23	22.4	21.6	21.3	21.1	–	–	–	–
36	0.949	p	6415	1.91	1.07	19.8	19.7	19.7	19.4	19.1	16.4	15.3	12.2	8.29

Note. [a]Redshift flag, *p* and *s* correspond to photometric and spectroscopic redshift, respectively. Photometric redshifts present a normalized standard deviation of $\sigma_{\mathrm{norm}} = 0.064$.

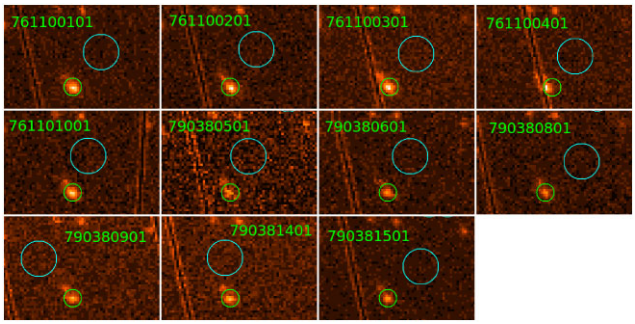

Figure 3. PN images in the 0.3–10 keV band of the 11 observations. The green and cyan circles with a radius of 15 and 30 arcsec, respectively, mark the position of the XID-7 source and the adopted used background region.

power-law models to obtain the best description of the spectral shape. The models used are as follows:

(i) `tbabs*powerlaw`
(ii) `tbabs*powerlaw*zphabs`
(iii) `tbabs*(powerlaw*zphabs + zgauss)`
(iv) `tbabs*((powerlaw + zbb)*zphabs + zgauss)`

We used an approach similar to that presented in previous X-ray analyses of bright AGNs (e.g. Corral et al. 2011; Iwasawa et al. 2020) with a high number of counts (>200). Our objective is to derive crucial parameters (Γ, N_{H}, and EW_{Fe}) essential for our study, avoiding the introduction of higher complexity in the form of additional components (e.g. ionized absorptions and reflected component).

The first base model consists of a simple power law (`powerlaw`) with a Galactic absorption (`tbabs`, Wilms, Allen & McCray 2000). The second model incorporates a neutral intrinsic absorber associated with the AGN or its host galaxy (`zphabs`). The third model increases the complexity of the second model by including a Fe−Kα emission line. For sources that were not well fit by our previous three models, we included a black body component (`zbb`) at temperature kT to account for the soft-excess emission.

In our analysis, we adopted a Galactic absorption of $N_H = 3.56 \times 10^{20}$ cm^{-2} in the line of sight of the X-ray field (as reported in Paper-I) and we let the power law and intrinsic absorption parameters free to vary. To ensure physically reliable estimations, we fixed the neutral emission line energy at $E = 6.4$ keV with a narrow line width at $\sigma = 0.01$ keV. Error bars for our spectral analysis were estimated with a 90 per cent confidence level. We employed a χ^2-statistics.

To assess whether there is an improvement in the accuracy of our results when we increase the complexity of the model, we employed the Akaike's Information Criterion (AIC, Akaike 1974) defined in equation (1). It is a statistical test for nested models that estimates the relative quality of our models (Hebbar et al. 2019; Krongold et al. 2021):

$$\mathrm{AIC} = 2k + \chi^2_{\mathrm{stat}}, \tag{1}$$

where χ^2_{stat} is the χ^2-statistic value and k is the number of parameters. Then, we estimated the relative likelihood (l_{AIC}) of our models using equation (2) to quantify if we are losing information due to excluding a new spectral component x_i. We used the inverse of l_{AIC} as the factor $\rho_{x_i} = l^{-1}_{\mathrm{AIC}}$ by which a more complex model with extra spectral components is preferred over a simpler model. A threshold of $\rho_{x_i} > 5$

Downloaded from https://academic.oup.com/mnras/article/532/2/1564/7706312 by Instituto Nac. de Astrofisica, optica y Electronica (INAOE) user on 11 July 2024

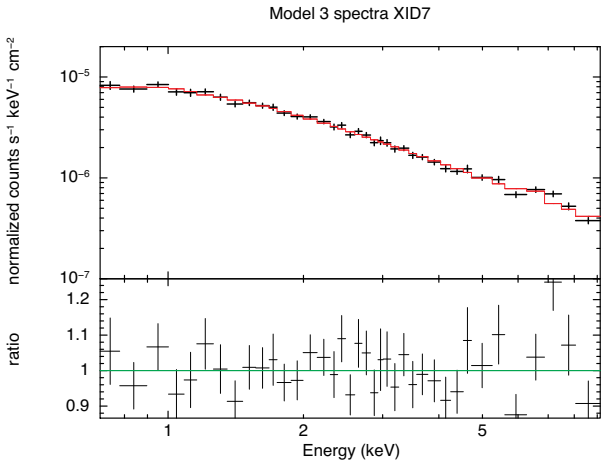

Figure 4. Upper: Combined rest-frame spectrum (black points) of the AGN XID-7. The red line represents the best-fitting model, i.e. `tbabs*(powerlaw*zphabs + zgauss)`. Lower: Residuals of the fit (data divided by the model).

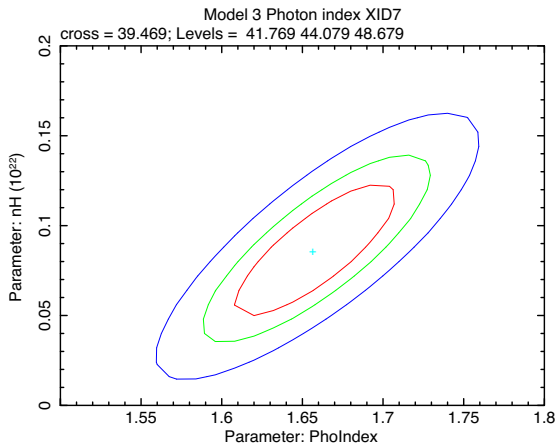

Figure 5. Confidence contours for the photon index and column density parameters derived by the best-fitting model applied to source XID-7. The red, green, and blue countors refer to 1σ, 2σ, and 3σ of confidence.

to confirm the detection of a new component was implemented.

$$l_{\rm AIC} = \exp\left(\frac{{\rm AIC}(x_0, x_i) - {\rm AIC}(x_0)}{2}\right). \quad (2)$$

We employed a 95 per cent of confidence for our statistical test. This threshold roughly corresponds to the 2σ level, supporting the use of the second model over the first to describe our data.

Fig. 4 presents an example of our analysis. In the upper panel, we display the combined 0.3–10 keV rest-frame spectrum (black dots) of the source XID-7, fitted with model 3 (red line). In the lower panel, we present the residuals (data divided by the folded model). We detected a residual feature at ~ 7 keV, which could be generated as a result of the Fe XXVI line at 6.97 keV. This component was not considered during our analysis. Then, in Fig. 5 we present the confidence contour plot of the photon index as a function of N_H for the source XID-7. The high counting statistics criterion allow us to reduce the degeneracy between the spectral parameters, Γ and N_H (Mateos et al. 2008).

A summary of the best-fitting parameters obtained with the spectral analysis of the 23 sources is presented in Table 2. The table includes values of χ^2 and degrees of freedom (dof) for the best-fitting model. Additionally, the results of the AIC criterion are provided in the ρ_{N_H} and ρ_{Fe} columns, respectively. Measurements of some properties such as Γ, N_H, kT, EW_{Fe}, and luminosities in the 2–10 keV band are also included.

Out of the 23 AGNs analysed, we found that 9 of them exhibit statistically significant intrinsic absorption component N_H, with a mean and standard deviation of $\log(N_H) = 20.92 \pm 0.18\,{\rm cm}^{-2}$. For the remaining 14 AGNs, we provide upper limits at 90 per cent of confidence level. We found statistically reliable detection of the Fe–Kα line for 12 AGNs, with a mean and standard deviation of their equivalent width of ${\rm EW_{Fe}} = 0.14 \pm 0.11$ keV. For the remaining 11, we have ${\rm EW_{Fe}}$ upper limits. The combined spectrum of each source fitted with its best model, according to the last column of Table 2, can be found in Appendix A in Figs A1 and A2. We obtained a mean photon index of $\Gamma = 1.88 \pm 0.16$ for the whole sample, estimated from the best-fitting model for each spectrum, which is a typical value for type-1 or unabsorbed AGNs (Mateos et al. 2010; Corral et al. 2011). Finally, we found that seven sources show an improvement with 90 per cent confidence when including a black body component (model 4).

4 CORRELATION ANALYSIS OF THE SPECTRAL PARAMETERS

To investigate the existence of physical correlations in our AGN sample, we performed a correlation analysis on their main spectral properties. In order to incorporate sources with upper limits in our ultra-narrow pencil beam survey, we employed a Monte-Carlo (MC) approach based on the linear regression algorithm proposed by Bianchi et al. (2007). The steps involved in the analysis are as follows:

(i) For each source, we generated a set of 1000 random values for the y-axis variable (e.g. $N_{\rm H}$ or Fe−K α). For sources with upper limits, we used a uniform distribution ranging from 0 to the upper limit, while for the remaining sources, we used a normal distribution with their errors as the standard deviation.

(ii) We computed a least-square linear regression fit for each set of the simulated data, considering one of the physical parameters of our AGN sample as the x-axis variable (e.g. z or L_x). The best fit and its statistical uncertainty will be determined as the mean and standard deviation, respectively, of the 1000 linear regressions.

(iii) To assess the strength of the correlations, we calculated the Spearman Rank Coefficient S and the $p_{\rm value}$ at the 95 per cent of confidence level to determine the statistical significance of any observed correlation (Zwillinger & Kokoska 2000).

The distributions obtained through the MC procedure reveal interesting relationships among the spectral properties of our sample, which will be presented next.

4.1 Iwasawa–Taniguchi effect

In Fig. 6, we present the distribution of the rest-frame X-ray luminosity at 2–10 keV energy band in units of 10^{44} erg s^{-1} versus ${\rm EW_{Fe}}$ of our sample in keV. We found an anticorrelation with a flat slope of $m = -0.17 \pm 0.08$ and Spearman rank of $S = -0.21$ with low significance $p_{\rm value} > 0.05$. However, when excluding sources with ${\rm EW_{Fe}}$ upper-limits (red triangles), the Spearman rank increases to $S = -0.6$ with a high significance of $p_{\rm value} < 0.05$. The best fit for the whole sample (black line) and only ${\rm EW_{Fe}}$ detections (red line) are expressed in equations (3) and (4), respectively:

Downloaded from https://academic.oup.com/mnras/article/532/2/1564/7706312 by Instituto Nac. de Astrofisica, optica y Electronica (INAOE) user on 11 July 2024

Table 2. Summary table of the spectral parameters with the power-law model of our bright AGN sample detected in the XMM−UNDF survey. We display the values obtained with the best-fitting model, which is reported in the last column with the digits 1, 2, 3, and 4. The results of the statistical test are presented in the columns ρ_{N_H} for the intrinsic absorption, and ρ_{N_H} for the Fe–Kα emission line. Only sources fitted with model 4 present kT measurements.

XID	χ^2/dof	ρ_{NH}	ρ_{Fe}	Γ	$\log(N_H)$ cm^{-2}	EW_{Fe} keV	kT keV	$\log(L_{2-10keV})$ erg s^{-1}	Best fit
1	47/49	33.28	2.65	$1.79^{+0.03}_{-0.03}$	$20.95^{+0.26}_{-0.51}$	< 0.01	–	$45.34^{+0.01}_{-0.01}$	2
2	49/25	2.72	8062.67	$2.03^{+0.05}_{-0.07}$	< 20	$0.32^{+0.2}_{-0.18}$	$0.15^{+0.03}_{-0.04}$	$42.48^{+0.02}_{-0.02}$	4
3	11/21	2.72	4.36E + 7	$1.91^{+0.09}_{-0.07}$	< 21	$0.31^{+0.15}_{-0.13}$	< 0.2	$44.32^{+0.01}_{-0.01}$	4
4	56/37	2.76	62.5	$2.06^{+0.05}_{-0.04}$	< 20.8	$0.06^{+0.04}_{-0.04}$	–	$44.45^{+0.01}_{-0.01}$	3
5	56/38	1.79E + 19	333.33	$1.49^{+0.04}_{-0.04}$	$21.30^{+0.08}_{-0.09}$	$0.07^{+0.04}_{-0.04}$	–	$44.12^{+0.01}_{-0.01}$	3
6	12/20	2.72	2.73	$1.86^{+0.06}_{-0.06}$	< 21.2	< 0.05	$0.17^{+0.09}_{-0.12}$	$44.35^{+0.01}_{-0.02}$	4
7	40/34	439.22	27.03	$1.65^{+0.05}_{-0.05}$	$20.93^{+0.17}_{-0.27}$	$0.06^{+0.05}_{-0.05}$	–	$44.11^{+0.01}_{-0.01}$	3
8	46/46	2.72	3.46	$1.67^{+0.03}_{-0.03}$	< 20.29	< 0.09	–	$43.58^{+0.01}_{-0.01}$	1
9	32/24	2.72	66.67	$1.92^{+0.09}_{-0.08}$	< 21.2	$0.09^{+0.07}_{-0.06}$	$0.14^{+0.11}_{-0.07}$	$44.22^{+0.01}_{-0.02}$	4
10	30/22	2.19E + 4	5.89	$1.87^{+0.07}_{-0.07}$	$20.97^{+0.14}_{-0.20}$	$0.06^{+0.09}_{-0.06}$	–	$43.94^{+0.01}_{-0.02}$	2
11	45/25	2.8	7.87	$2.07^{+0.08}_{-0.04}$	< 20.3	$0.31^{+0.38}_{-0.30}$	–	$41.94^{+0.03}_{-0.02}$	3
12	28/25	1502.67	2.72	$2.01^{+0.06}_{-0.06}$	$20.74^{+0.20}_{-0.23}$	< 0.07	–	$43.71^{+0.02}_{-0.02}$	2
13	34/29	2.72	3.7	$1.81^{+0.04}_{-0.04}$	< 20.3	< 0.09	–	$43.81^{+0.01}_{-0.02}$	1
14	19/21	2.76	10.75	$1.94^{+0.08}_{-0.05}$	< 20.9	$0.06^{+0.05}_{-0.04}$	–	$44.31^{+0.01}_{-0.02}$	3
15	39/31	2.82	5.71	$1.92^{+0.07}_{-0.03}$	< 20.3	$0.10^{+0.25}_{-0.09}$	–	$43.05^{+0.02}_{-0.02}$	1
16	17/18	2.72	5.41	$1.93^{+0.13}_{-0.08}$	< 20.1	< 0.23	$0.14^{+0.03}_{-0.04}$	$43.09^{+0.02}_{-0.02}$	4
17	20/22	314.19	2.72	$1.73^{+0.07}_{-0.07}$	$20.67^{+0.21}_{-0.24}$	< 0.12	–	$43.05^{+0.02}_{-0.02}$	2
18	44/21	2.72	2.73	$2.04^{+0.07}_{-0.05}$	< 20.65	< 0.09	< 0.2	$43.42^{+0.02}_{-0.02}$	4
19	28/27	2.02E + 10	2.25	$1.86^{+0.07}_{-0.06}$	$20.95^{+0.12}_{-0.11}$	< 0.12	–	$43.19^{+0.03}_{-0.02}$	2
20	43/33	3.14E + 4	2.72	$1.67^{+0.06}_{-0.06}$	$20.90^{+0.18}_{-0.17}$	< 0.16	–	$43.43^{+0.02}_{-0.02}$	2
28	14/22	2.72	250	$1.88^{+0.12}_{-0.12}$	< 21.16	$0.16^{+0.15}_{-0.14}$	$0.13^{+0.05}_{-0.05}$	$43.42^{+0.02}_{-0.03}$	4
33	26/22	3944.19	2.72	$2.02^{+0.11}_{-0.11}$	$20.87^{+0.25}_{-0.12}$	< 0.27	–	$42.82^{+0.04}_{-0.03}$	2
36	20/24	2.72	5.02	$2.22^{+0.08}_{-0.08}$	< 20.85	$0.08^{+0.26}_{-0.07}$	–	$43.48^{+0.03}_{-0.03}$	1

$$\log\left(\frac{\mathrm{EW_{Fe}}}{\mathrm{keV}}\right)_{\mathrm{all}} = (-1.28 \pm 0.08) + (-0.17 \pm 0.08)\log\left(\frac{Lx}{10^{44}\,\mathrm{erg\,s^{-1}}}\right), \tag{3}$$

$$\log\left(\frac{\mathrm{EW_{Fe}}}{\mathrm{keV}}\right)_{\mathrm{det}} = (-1.10 \pm 0.06) + (-0.23 \pm 0.07)\log\left(\frac{Lx}{10^{44}\mathrm{erg\,s^{-1}}}\right). \tag{4}$$

Our results agree with the observed $L_x - EW_{\mathrm{Fe}}$ anticorrelation reported in previous studies. For instance, Bianchi et al. (2007) found a similar trend for nearby AGNs (blue dotted line), while Ricci et al. (2014) observed this effect in two samples of Seyfert-2 and Seyfert-1 galaxies (grey points and dotted line) with a slope of $m = 0.18 \pm 0.06$. They also included upper limits with their best fits in agreement with our results.

The underlying physical mechanism responsible for the 'Iwasawa–Taniguchi effect' (Iwasawa & Taniguchi 1993) remains unknown. One potential explanation is that brighter AGNs may induce higher degrees of ionization in the surrounding material, resulting in the fading of the fluorescence Fe–Kα line emitted by low-ionization matter (Shu et al. 2010). Furthermore, the iron emission originating from cooler gas near the supermassive black hole could undergo scattering due to radiation pressure or thermal dissipation (e.g. Fabian, Vasudevan & Gandhi 2008). Alternatively, it is plausible that the decrease in the torus covering factor and/or column density of the cold gas responsible for the iron emission is correlated with an increase in AGN luminosity. This suggests that as the luminosity of the AGN rises, the covering factor and/or column density of the cold gas in the torus declines (Bianchi et al. 2007; Ricci et al. 2014).

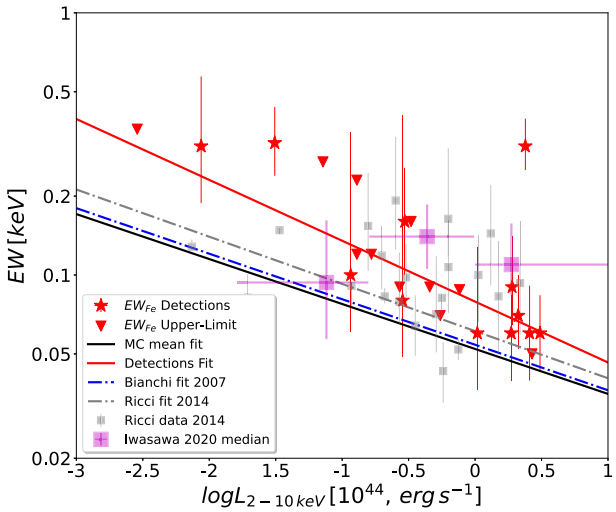

Figure 6. Fe−Kα Equivalent Width versus the X-ray luminosity at 2–10 keV energy band of our AGN sample. The black and red lines represent the best MC linear fit for the whole sample and the Fe–Kα detections (red star), respectively. We included the data and results of previous works of Bianchi et al. (2007) (blue line), Ricci et al. (2014) (grey line and points), and Iwasawa et al. (2020) (pink squares).

4.2 Intrinsic column density versus redshift

Observational results and synthesis models have shown that obscured AGNs represent a significant fraction of the entire AGN population,

Downloaded from https://academic.oup.com/mnras/article/532/2/1564/7706312 by Instituto Nac. de Astrofisica, optica y Electronica (INAOE) user on 11 July 2024

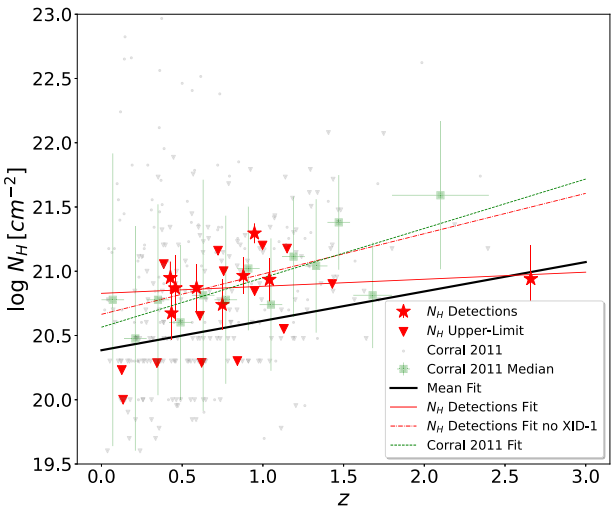

Figure 7. Redshift versus intrinsic column density absorption of our bright AGN sample. The black and red solid lines correspond to the best fit for the whole sample and only the N_H detections (red star), respectively. The gray points and green squares refer to the XBS AGN sample reported by Corral et al. (2011) with its corresponding best fit (green dark dashed line). The red dotted line corresponds to the best fit of the N_H detections after removing the XID-1 source at $z = 2.66$.

which increases with redshift (D'Amato et al. 2020). For instance, Gilli et al. (2007) and Burlon et al. (2011) estimated that the fraction of Compton-thick AGNs ($N_H \geq 1.5 \times 10^{24}\ cm^{-2}$) in the local universe comprises about 20 per cent to 30 per cent of the total AGN population.

In our analysis presented in Fig. 7, we did not find a significant correlation ($p_{\rm value} > 0.05$) with Spearman rank of $S \approx 0.23$ between the intrinsic absorption $N_{\rm H}$ of our AGN sample as a function of the redshift. This result could be due to the limited redshift range covered for our data. For instance, our AGN sample includes only one high-redshift source, the XID-1 at $z = 2.66$. Due to the lack of more sources to sample this high-redshift regime, the best fit for the hole sample (black solid line) and the N_H detection (red solid line) might be dominated by this AGN, resulting in misleading results. In the case of removing the highest redshift source, we found a moderate ($S = 0.45$) but still low significant ($p_{\rm value} > 0.05$) correlation where the linear fit (red-dotted line) increases from a flat $m \approx 0.05$ to a steeper slope $m = 0.31$, expressed by the equation:

$$\log(N_H) = (20.66 \pm 0.16) + (0.31 \pm 0.23)z \tag{5}$$

We compared our results with a set of AGNs detected in the *XMM−Newton* Bright Serendipitous Survey (XBS; Corral et al. 2011). The XBS is composed of 305 AGNs (grey dots) detected in a sky coverage of 28.1 deg^2 and flux limit of 7×10^{-14} erg cm^{-2} s^{-1} (Della Ceca et al. 2004). Most of the AGNs detected in the XBS are distributed in the range of $z = 0$–1.5 (293 out of 305) with bright X-ray sources similar to our survey. To analyse the XBS catalogue, we computed the median and standard deviation in 13 redshift bins of $\Delta z = 0.14$ with at least 15 elements per bin, except for the last two bins at $z > 1.5$ with $\Delta z = 0.24$ and 0.6, respectively, both with 6 elements each. We found a strong and statistically reliable correlation (green dotted line) with $S = 0.761$ and $p_{\rm value} = 0.003$ that agrees with the linear fit obtained from our AGNs with intrinsic absorption, after removing the source with the highest redshift.

The observed column densities could be associated with various factors, such as the presence of dust lanes in the host galaxy or underlying presence of BAL QSOs. For sources at higher redshift ($z > 3$, see Gilli et al. 2022), the underlying physical mechanism driving this behavior could be related to the increase of the reservoir of gas available towards early cosmic epochs, leading to an evolution of the fraction of obscured AGNs, as reported by Liu et al. (2017) and Iwasawa et al. (2020) with the 7Ms Chandra Deep Field-South Survey (CDFS).

We investigated some other physical relationships, such as EW$_{\rm Fe}$ versus $N_{\rm H}$, L_x versus $N_{\rm H}$, and EW$_{\rm Fe}$ versus redshift. We observed no significant correlation between EW$_{\rm Fe}$ and N$_{\rm H}$, as well as between L_x and $N_{\rm H}$. However, we detected a significant anticorrelation between EW$_{\rm Fe}$ and z, which could be explained by the EW$_{\rm Fe}$–L_x relation presented in Section 4.1, i.e. at higher redshifts, we observe intrinsically more luminous sources with lower EW$_{\rm Fe}$, following the Iwasawa−Taniguchi effect.

5 X-RAY VARIABILITY AND BLACK HOLE MASS−LUMINOSITY RELATION

5.1 The normal excess variances

Since we are working with multi-epoch observations, we can study how the X-ray variability of our sample evolves as a function of their SMBH mass. Following Lanzuisi et al. (2014), we used the Normal Excess Variances $\sigma^2_{\rm rms}$ to measure the amplitude flux variation of our AGN sample, as follows:

$$\sigma^2_{\rm rms} = \frac{1}{(N_{\rm obs}-1)\bar{x}^2}\sum_{i=1}^{N_{\rm obs}}(x-\bar{x})^2 - \frac{1}{N_{\rm obs}\bar{x}^2}\sum_{i=1}^{N_{\rm obs}}\sigma^2_{{\rm err},i} \tag{6}$$

where N_{obs} is the number of observations, $\bar{x}$ is the average flux of the source in the full survey, and x_i is the individual flux per observation with error $\sigma_{{\rm err},i}$. The Normal Excess error err($\sigma^2_{\rm rms}$) is defined as follows:

$$\mathrm{err}(\sigma^2_{\rm rms}) = \sqrt{\left(\sqrt{\frac{2}{N_{\rm obs}}}\frac{\overline{\sigma^2_{\rm err}}}{\bar{x}^2}\right)^2 + \left(\sqrt{\frac{\overline{\sigma^2_{\rm err}}}{N_{\rm obs}}}\frac{2F_{\rm var}}{\bar{x}}\right)^2}, \tag{7}$$

where $F_{\rm var} = \sqrt{\sigma^2_{\rm rms}}$ is the fractional variability and the component $\overline{\sigma^2_{\rm err}} = \frac{1}{N_{\rm obs}}\sum_{i=1}^{N}\sigma^2_{{\rm err},i}$ is the mean square error. For those sources that err($\sigma^2_{\rm rms}$) $> \sigma^2_{\rm rms}$, we will use only their upper limit, which is defined as $\sigma^2_{\rm rms,UL} = \sigma^2_{\rm rms} + \mathrm{err}(\sigma^2_{\rm rms})$.

To include those sources with upper limits, we employed the same MC linear regression simulation, as described before. Our results are presented in Table 3. We found an average Excess Variance for the whole bright AGN sample of $\sigma^2_{\rm rms} = 0.091 \pm 0.028$.

We did not detect a relation between $\sigma^2_{\rm rms}$ and the X-ray counts. This suggests that our sample possesses a sufficient number of counts to have a statistically reliable measure of the excess variance. For example, Lanzuisi et al. (2014) found an anticorrelation between $\sigma^2_{\rm rms}$ and the average X-ray counts. They reported that this anticorrelation arises due to a selection effect that disappears within their brightest AGN sample.

5.2 The BH mass estimation

Since we do not possess optical spectroscopic data for most of our sources, we do not have measurements of optical lines such as Mg IIλ2798 Å , C IVλ1549 Å , H β, or H α. Therefore, we decided to use two indirect methods to estimate the SMBH mass of our AGN sample and subsequently compare the results.

Downloaded from https://academic.oup.com/mnras/article/532/2/1564/7706312 by Instituto Nac. de Astrofisica, optica y Electronica (INAOE) user on 11 July 2024

Table 3. Summary table of the spectral parameters with the BMC model and the black hole masses estimated with both methods.

XID	$\Gamma^a_{\rm BMC}$	$\log(A)$	$N^b_{\rm BMC}$ (10^{-6})	χ^2/dof	$\log(L_{5100})^c$ (erg s^{-1})	$\log(M_{\rm BH),X})^d$ (erg s^{-1})	$\log(M_{{\rm BH},L_x})^e$ ($M_\odot$)	$\sigma^2_{\rm rms}$ ($M_\odot$)
1	1.82 ± 0.04	5.44	0.96 ± 0.03	39/41	46.7	8.63 ± 0.06	8.94 ± 0.19	0.031 ± 0.004
2	1.77 ± 0.07	1.17	0.47 ± 0.04	11/5	42.7	6.31 ± 0.07	6.68 ± 0.21	0.370 ± 0.032
3	1.74 ± 0.04	0.98	0.68 ± 0.02	20/6	45.2	7.87 ± 0.06	8.13 ± 0.10	0.011 ± 0.017
4	2.00 ± 0.05	−1.41	0.48 ± 0.16	43/24	45.4	7.80 ± 0.13	8.23 ± 0.11	0.020 ± 0.006
5	1.55 ± 0.06	1.11	0.31 ± 0.01	35/22	45	7.93 ± 0.12	7.97 ± 0.08	0.020 ± 0.007
6	1.84 ± 0.04	7.04	0.28 ± 0.01	9/10	45.3	7.66 ± 0.06	8.16 ± 0.10	0.016 ± 0.015
7	1.62 ± 0.08	0.87	0.55 ± 0.02	34/20	45	7.75 ± 0.10	7.97 ± 0.08	0.067 ± 0.018
8	1.66 ± 0.06	0.90	0.20	25/23	44.2	7.3	7.55 ± 0.11	0.364 ± 0.059
9	1.78 ± 0.06	−0.56	1.23 ± 0.35	16/11	45.1	8.26 ± 0.09	8.06 ± 0.09	0.049 ± 0.022
10	1.81 ± 0.06	1.12	0.22	16/7	44.7	7.4 ± 0.4	7.83 ± 0.08	0.156 ± 0.031
11	1.83 ± 0.11	1.39	0.16 ± 0.03	10/5	41.9	5.74 ± 0.08	6.25 ± 0.26	0.032 ± 0.022
12	2.03 ± 0.07	7.22	0.21	9/8	44.4	7.1 ± 0.6	7.65 ± 0.10	0.028 ± 0.016
13	1.74 ± 0.06	−0.49	0.63 ± 0.34	13/11	44.5	7.90 ± 0.13	7.73 ± 0.09	0.078 ± 0.027
14	1.94 ± 0.04	7.34	0.18 ± 0.02	17/11	45.2	7.48 ± 0.07	8.12 ± 0.10	0.070 ± 0.024
15	1.74 ± 0.09	0.75	0.23 ± 0.03	7/7	43.5	6.79 ± 0.08	7.13 ± 0.16	0.448 ± 0.175
16	1.95 ± 0.10	1.25	0.23 ± 0.03	3/2	43.5	6.67 ± 0.19	7.16 ± 0.15	0.040 ± 0.023
17	1.76 ± 0.08	0.98	0.13	8/4	43.5	7.0	7.13 ± 0.16	0.058 ± 0.024
18	1.73 ± 0.08	0.99	0.14	16/6	44	7.0	7.42 ± 0.12	0.030 ± 0.023
19	1.90 ± 0.07	6.62	0.20 ± 0.05	14/7	43.7	6.76 ± 0.09	7.24 ± 0.14	0.041 ± 0.019
20	1.79 ± 0.07	1.04	3.03 ± 0.01	14/13	44	7.04 ± 0.07	7.43 ± 0.12	0.018 ± 0.010
28	1.78 ± 0.10	0.82	0.10	10/8	44	7.0	7.42 ± 0.12	0.030 ± 0.017
33	2.07 ± 0.15	4.94	0.09 ± 0.04	5/6	43.2	6.29 ± 0.18	6.95 ± 0.18	0.047 ± 0.025
36	1.97 ± 0.15	1.62	0.20 ± 0.15	9/7	44.1	7.25 ± 0.22	7.47 ± 0.12	0.156 ± 0.047

Note. [a]Related to the spectral index α with the equation $\alpha = \Gamma_{\rm BMC} - 1$. [b]BMC normalization with uncertainties at 1σ of confidence. [c] Inferred optical continuum at 5100 Å, estimated from equation (8). [d]AGN black hole masses computed with equation (9) as a function of L_{5100}. [e] AGN black hole masses computed with the spectral parameters including the BMC model with equation (11).

5.2.1 *Estimating the BH mass from X-ray luminosity, M_{BH,L_x}*

The first method involved the X-ray luminosity in the 2–10 keV energy band with equation (8) to estimate the optical continuum at 5100 Å (L_{5100}). This equation was derived by Netzer (2019), from the tight correlation between the UV and X-ray luminosities $\alpha_{\rm OX}$ and arises from theoretical calculations of optically thick, geometrically thin accretion disks, and observations of X-ray properties in type-1 AGN. According to the estimated column densities, we can classify our sources into this class.

$$\log(L_{5100}) = 1.4 \times \log(L_{2-10\,{\rm keV}}) - 16.8. \quad (8)$$

Then, we estimated the BH masses ($M_{{\rm BH},L_x}$) for the whole sample using the $M_{\rm BH} - L_{5100}$ empirical relation described in equation (9), which was originally reported by Peterson et al. (2004) based on black hole mass measurements using reverberation analysis in AGNs. We found a mean and standard deviation of $\log(M_{{\rm BH},L_x}/{\rm M}_\odot) = 7.59 \pm 0.59$ (see Table 3):

$$\log\left(\frac{M}{10^8\,{\rm M}_\odot}\right) = -0.12(\pm 0.07) + 0.79(\pm 0.09)\log\left(\frac{L_{5100}}{10^{44}\,{\rm erg\,s^{-1}}}\right). \quad (9)$$

5.2.2 *Estimating the BH mass from X-ray scaling, $M_{\rm BH,X}$*

For the second method, we used the X-ray scaling estimation technique (Gliozzi et al. 2011; Gliozzi, Williams & Michel 2021). This approach scaled the spectral parameters of our sample with a set of reference sources with known mass and distance, allowing us to estimate the AGNs black hole mass. Gliozzi et al. (2011) tested this method using a set of AGN black hole masses estimated from reverberation mapping. They reported a strong agreement between their estimation and those from reverberation mapping.

During our analysis, we have already fitted our spectra with a combination of a simple power law, a Galactic absorption, a free-to-vary intrinsic absorption, and a narrow gaussian at fixed rest-frame energy of 6.4 keV for an iron line. However, to estimate $M_{\rm BH}$ using the X-ray scaling method, we need to refit our spectra while including the Bulk Motion Comptonization model (BMC). The BMC model is designed for modeling X-ray spectra of accreting black holes and consists of the convolution of thermal seed photons producing a power law. This model comprises four parameters, the BMC normalization $N_{\rm BMC}$, the photon temperature kT, the spectral index $\alpha = \Gamma_{\rm BMC} - 1$ where $\Gamma_{\rm BMC}$ is the photon index, and the parameter $\log(A)$ is the so-called 'illumination factor' related to the fraction of scattered seed photons f, i.e. f is the ratio between the number of Compton scattered photons and the number of seed photons, described by the equation $f = A/(1 + A)$ (Shrader & Titarchuk 2003; Farinelli et al. 2008; Shaposhnikov & Titarchuk 2009; Williams et al. 2023).

The considerations that support this method for accreting compact objects, presented by Shaposhnikov & Titarchuk (2009) and Gliozzi et al. (2011), can be summarized as follows: (1) The break frequency X-ray variability of the power spectrum is inversely proportional to the black hole mass. (2) The BMC normalization is proportional to the distance and luminosity, i.e. $N_{\rm BMC} \propto L/d^2$. (3) The luminosity of an accreting BH can be expressed as $L \propto \eta M_{\rm BH}\dot{m}$, where η describe the radiative efficiency and $\dot{m}$ the accretion rate. (4) Γ is a reliable indicator for the source's spectral state regardless of the BH mass (Shaposhnikov & Titarchuk 2009).

Following the methodology described in Gliozzi et al. (2021), the black hole mass is estimated in three steps. First, we have to estimate N_{BMC} from our refitting process, which is performed in the 2–10 keV energy range to avoid the complexity associated with the soft X-ray band, such as the soft excess (e.g. observed in seven sources) and the

Downloaded from https://academic.oup.com/mnras/article/532/2/1564/7706312 by Instituto Nac. de Astrofisica, optica y Electronica (INAOE) user on 11 July 2024

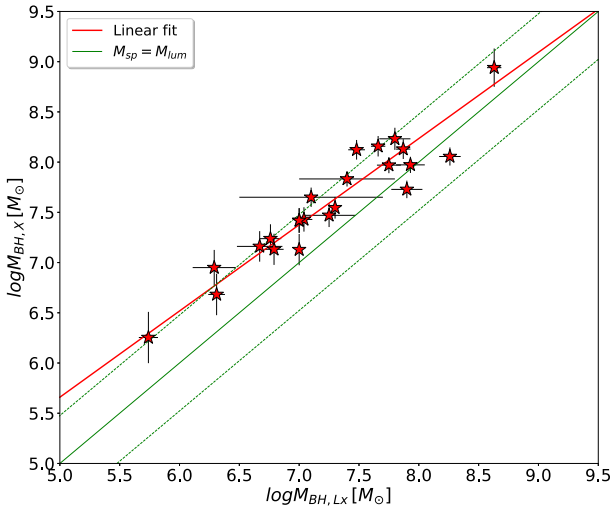

Figure 8. BH masses comparison between the X-ray scaling method (Section 5.2.1) versus the luminosity method (Section 5.2.2). The red and green solid lines represent the best linear fit and a perfect one-to-one correspondence, respectively, while the dashed green lines indicate the ratios of 3 and 1/3.

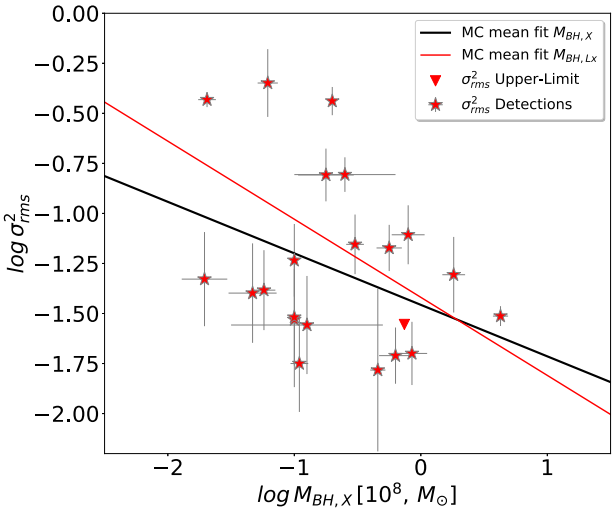

Figure 9. Distribution of $\sigma^2_{\rm rms}$ versus $M_{{\rm BH},X}$ of our AGN sample. The best MC linear fit is presented with the black solid line, while the red line is obtained with $M_{{\rm BH},L_x}$.

potential presence of warm absorbers. We used the best fit obtained from Section 3.2; however, we replaced the `powerlaw` component with the BMC model (e.g. `tbabs*BMC*zphabs`).

The BMC parameters are free to vary (N_{BMC}, log(A), α), except for kT, which was fixed to 0.1 keV based on the result obtained by Gliozzi et al. (2011) with their set of AGNs, and we used the value of log(A) from the first fit iteration. They reported that the parameters kT and log(A) have a negligible effect on the estimation of $M_{\rm BH}$.

The second step consists of computing the BMC normalization of the reference sources ($N_{{\rm BMC},r}$) with equation (10). These reference sources served as calibrations and comprised Galactic stellar-mass black holes with known masses and distances:

$$N_{{\rm BMC},r}(\Gamma_{\rm BMC}) = N_{\rm tr} \times \left(1 - \ln\left[e^{\frac{a-\Gamma_{\rm BMC}}{B}} - 1\right]\right)^{1/\beta}, \quad (10)$$

where $\Gamma_{\rm BMC}$ is obtained from the spectral index α, while a, B, N_{tr}, and β are the reference sources patterns reported by Gliozzi et al. (2011) and presented in their table 2. Finally, we used the equation (11) to estimate the black hole masses of our sample:

$$M_{{\rm BH},t} = M_{{\rm BH},r} \times \left(\frac{N_{{\rm BMC},t}}{N_{{\rm BMC},r}}\right) \times \left(\frac{d_t}{d_r}\right)^2, \quad (11)$$

where d is the distance and the t and r subscripts denote the target and the reference source, respectively. The best estimation of $M_{\rm BH}$ will be the average of the masses inferred from all the available reference sources. Using the X-ray scaling method, we obtained a mean SMBH mass of $\log(M_{{\rm BH},X}/{\rm M}_\odot) = 7.26 \pm 0.68$ for the entire AGN sample.

Fig. 8 presents a comparison between $M_{{\rm BH},L_x}$ and $M_{{\rm BH},X}$, where we observed a trend of lower masses for the luminosity method, described as $M_{{\rm BH},L_x} \sim 0.33 \times M_{{\rm BH},X}$. The red and green solid lines represent the best fit and the ideal case when $M_{{\rm BH},X} = M_{{\rm BH},L_x}$, respectively. A summary of our spectral results and the BH mass estimations are provided in Table 3 [see also Mathur, Kuraszkiewicz & Czerny (2001) for measuring $M_{{\rm BH},X}$].

It is important to highlight that the masses estimated in this paper are based on spectral and luminosity measurements. Therefore, caution should be taken when interpreting the outcome of the relations derived for BH mass with the other parameters in the following sections.

5.3 Normal excess variance versus BH mass and luminosity

In this section, we studied how and if the X-ray variability of our AGN sample correlates with the X-ray luminosity and black hole mass. For this analysis, we did not include the source XID-11 because it is an outlier due to its lower mass, i.e. $\log(M_{{\rm BH},X}/{\rm M}_\odot) < 6$.

In Fig. 9, we present the Normal Excess Variance versus the Black Hole masses of our sample. The red and black solid lines represent the best MC linear fit using $M_{{\rm BH},L_x}$ (equation 12) and $M_{{\rm BH},X}$ (equation (13)), respectively. In both cases, we found an anticorrelation with a reliable confidence level ($p_{\rm value} \approx 0.05$). For the $\sigma^2_{\rm rms} - M_{{\rm BH},L_x}$ relation we obtained a slope of $m = -0.39 \pm 0.06$ and Spearman rank coefficient of $S = -0.34$, while the $\sigma^2_{\rm rms} - M_{{\rm BH},X}$ relation exhibits a flatter slope of $m = -0.26 \pm 0.05$ and $S = -0.26$:

$$\log(\sigma^2_{\rm rms}) = (-1.42 \pm 0.04) + (-0.39 \pm 0.06)\log\left(\frac{M_{{\rm BH},L_x}}{10^8\,{\rm M}_\odot},\right) \quad (12)$$

$$\log(\sigma^2_{\rm rms}) = (-1.46 \pm 0.05) + (-0.26 \pm 0.05)\log\left(\frac{M_{{\rm BH},X}}{10^8\,{\rm M}_\odot}\right). \quad (13)$$

Since our results are consistent with both methods and to reduce potential biases, for the remaining analysis, including the study of the Eddington ratio distribution in Section 6, we will use only the masses estimated from the X-ray Scaling Method.

In Fig. 10, we present the distribution of σ^2_{rms} as a function of the rest-frame X-ray luminosity at $2-10$ keV energy range. A statistically significant 'variability–luminosity' anticorrelation is observed, presented with the black solid line expressed in equation (14), with Spearman rank of $S \approx -0.4$. Additionally, the obtained linear fit closely aligns with the purple dotted line, which corresponds to the best MC linear fit (with arbitrary y-axis interceptions) obtained with $\sigma^2_{\rm rms}$–$M_{{\rm BH},X}$ relation. For instance, the slope of the bright sample is $m = -0.31 \pm 0.04$, which is similar (considering the errors) to the fit obtained with the $\sigma^2_{\rm rms}$–$M_{{\rm BH},X}$ relation, i.e. a slope

Downloaded from https://academic.oup.com/mnras/article/532/2/1564/7706312 by Instituto Nac. de Astrofisica, optica y Electronica (INAOE) user on 11 July 2024

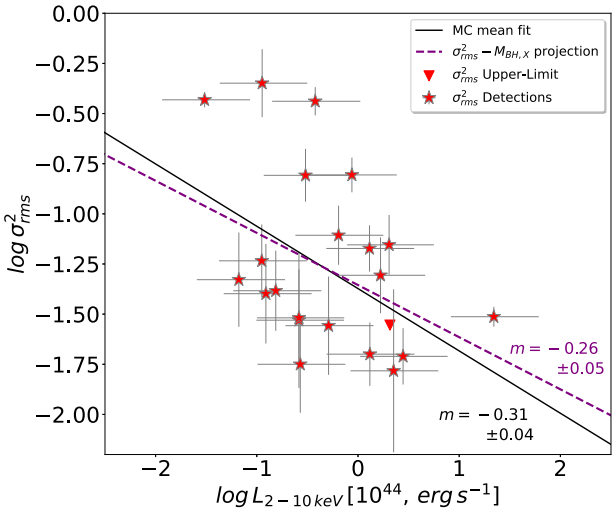

Figure 10. Normal excess variances versus X-ray luminosity of our AGN sample with measurements of their rest-frame X-ray luminosity at 2–10 keV energy range. The best MC linear fit is presented with the black line, while the purple dotted line represents the best MC linear fit (with arbitrary *y*-axis interceptions) obtained with the $\sigma^2_{rms} - M_{BH,X}$ relation.

of $m = -0.26 \pm 0.05$:

$$\log(\sigma^2_{\rm rms}) = (-1.37 \pm 0.04) + (-0.31 \pm 0.04) \log\left(\frac{L_{2\text{–}10\,\rm keV}}{10^{44}\,\rm erg\,s^{-1}}.\right) \tag{14}$$

Furthermore, we tested this relation with the full AGN population detected in the XMM–UNDF (i.e. 160 AGNs detected in at least three observations). We found that this anticorrelation did not change when considering a larger sample, maintaining the same trend with a slope of $m = -0.3 \pm 0.03$. Our results agree with the reported by previous deep X-ray surveys (e.g. Papadakis et al. 2008; Zheng et al. 2017), and for local (e.g. Ponti et al. 2012) and distance (e.g. Yang et al. 2016) AGNs samples.

5.3.1 An underlying M_{BH} dependence

We obtained consistent slopes for both relations, with $m = -0.26 \pm 0.05$ for $\sigma^2_{rms} - M_{BH}$ and $m = -0.31 \pm 0.04$ for $\sigma^2_{rms} - L_x$, respectively. These results support the idea that the 'Luminosity–X-ray variability' anticorrelation is generated as a byproduct of an intrinsic 'BH mass–X-ray variability' relation. Furthermore, our results agree with those reported from previous surveys as Papadakis et al. (2008), Ponti et al. (2012), and Lanzuisi et al. (2014). For example, Papadakis et al. studied the variability–luminosity relation as a function of the redshift with a set of AGNs detected in the Lockman Hole, they found that this relationship with a steeper slope of $m = -0.66 \pm 0.12$ increases with redshift up to $z \sim 1$ and then stays roughly constant. Similarly, Lanzuisi et al. with the XMM-COSMOS survey with a larger sample made by 638 AGNs, reported roughly the same reliable anticorrelations with a flatter slope of $m = -0.23 \pm 0.03$ and Spearman coefficient of $S = -0.38$ for both L_x–$\sigma^2_{\rm rms}$ and $M_{\rm BH} - \sigma^2_{\rm rms}$.

A feasible scenario that could cause these relations can be explained as follows: during the accretion process when a gas particle with mass m_i interacts with the black hole, the released energy $E_{\rm accretion}$ is proportional to the black hole mass and therefore for the size of the emitting region, given by $\Delta E_{\rm accretion} = GM_{\rm BH}m_i/R_s$ (where R_s is the Schwarzschild radius). Most of this energy is emitted as optical and UV photons. These seed photons are then reprocessed by the hot corona generating the observed AGN X-ray luminosity. Since the time scales associated with the accretion disc (e.g. viscous time and Sound-crossing time[4]) are proportional to the BH mass (Peterson et al. 2004), variations in the accretion rate will primarily drive the AGN flux variability (Uttley & Casella 2014; Ricci & Trakhtenbrot 2023). Therefore, low-mass BHs (corresponding to faint AGNs) will have shorter time scales, leading to higher variations in the accretion rate and, as a result, affect the general flux emission of the AGN producing high variability, and vice versa high-mass BHs (corresponding to bright AGNs) will display lower variability due to longer time-scales.

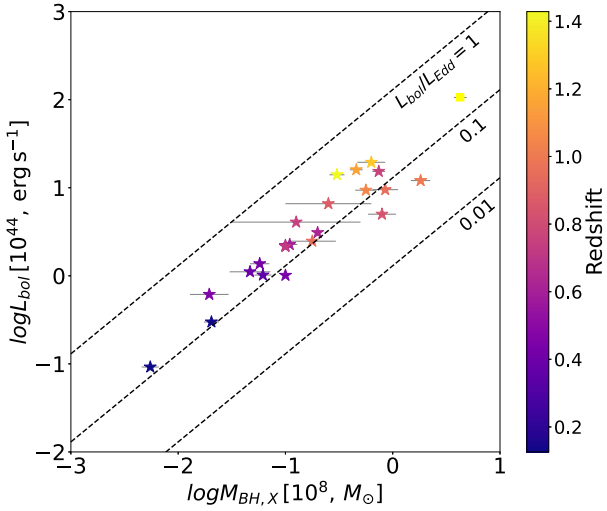

Figure 11. $L_{\rm bol}$ versus $M_{\rm BH,X}$ distribution of our AGN sample weighted by their redshift (colour bar). The yellow square represents the AGN XID-1 at $z = 2.66$.

6 THE EDDINGTON RATIO DISTRIBUTION

Another important parameter that we analysed in this paper is the Eddington ratio ($\lambda_{\rm Edd}$), which is defined as the ratio between the bolometric luminosity ($L_{\rm bol}$) and the Eddington luminosity ($L_{\rm Edd}$). $\lambda_{\rm Edd}$ represents the accretion rate relative to the Eddington limit and is a measure of how efficiently material is converted into radiation. We used $L_{2-10\,\rm keV}$ to infer $L_{\rm bol}$ from the X-ray luminosities. Following Netzer (2013, 2019), we used $L_{\rm bol} = K_{\rm bol} \times L_{2-10\,\rm keV}$, where $K_{\rm bol}$ is the bolometric correction factor defined as $K_{\rm bol} = 69.8 - 1.4\log(L_{2-10\,\rm keV}/\rm erg\,s^{-1})$.

Fig.11 presents the distribution of $L_{\rm bol}$ and $M_{\rm BH,X}$ of our AGN sample. We observed a broad range of bolometric luminosities of $42.5 < \log(L_{\rm bol}) < 46.1$ with low dispersion of the BH masses at different redshift bins. For a better visualization of the redshift distribution, the colour bar did not consider the AGN with the highest redshift ($z \sim 2.6$) marked with the yellow square. The multiple linear regression equation of $L_{\rm bol}$ as a function of $M_{\rm BH}$ and z is expressed

[4]The viscous time represents the time it takes for accretion rate variations to propagate across the disk, while the Sound-crossing time represents the time it takes for mechanical instabilities to cross the disc as acoustic waves, travelling at the sound speed (Peterson et al. 2004).

Downloaded from https://academic.oup.com/mnras/article/532/2/1564/7706312 by Instituto Nac. de Astrofisica, optica y Electronica (INAOE) user on 11 July 2024

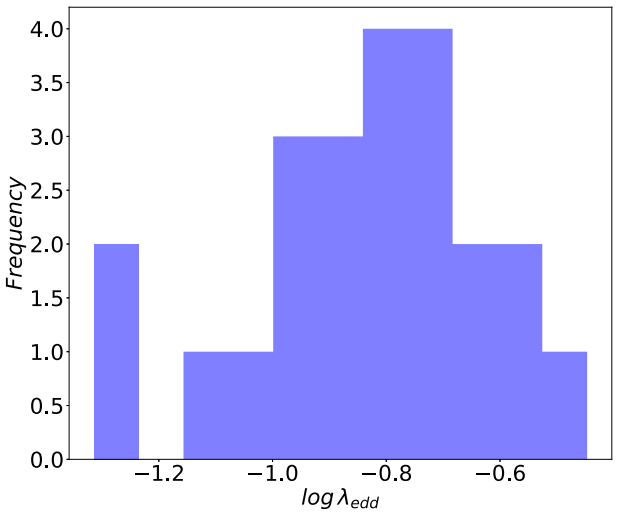

Figure 12. Eddington ratio histogram of our AGN sample.

as follows:

$$\log\left(\frac{L_{\rm bol}}{10^{44}\,{\rm erg}\,s^{-1}}\right) = (0.39 \pm 0.19) + (0.75 \pm 0.17)\log\left(\frac{M_{\rm BH}}{10^{8}\,{\rm M}_{\odot}}\right) + (0.57 \pm 0.10)z \quad (15)$$

For an in-falling plasma composed mostly of ionized hydrogen, the Eddington luminosity can be calculated as $L_{\rm Edd} \approx 1.3 \times 10^{38}(M_{\rm BH}/{\rm M}_{\odot})\,{\rm erg\,s^{-1}}$ (Rees 1978). Fig. 12 presents the Eddington ratio distribution of our sample, revealing a lognormal shape with a tail in the lowest values. We found that most of our AGNs are relatively low accretion rate systems with $\lambda_{\rm Edd} < 0.3$, having a mean of 0.16 and a dispersion of 0.07 dex. In Table 4, we summarize the estimation of $L_{\rm bol}$, $L_{\rm Edd}$ and $\lambda_{\rm Edd}$. Our result is not unexpected since Seyfert galaxies tend to have relatively low (~ 0.1) Eddington ratios (e.g. Nobuta et al. 2012; Caccianiga et al. 2013). For instance, Caccianiga et al. (2013) reported that most of their flux-limited sample, composed of 154 type-1 AGNs at redshift from 0.02 to

Table 4. Summary table of the $L_{\rm bol}$, $L_{\rm Edd}$, and $\lambda_{\rm Edd}$ parameters, estimated from our AGN sample.

XID	$\lambda_{\rm Edd}$	$L_{\rm edd}$ 10^{44} erg s^{-1}	$L_{\rm bol}$ 10^{44} erg s^{-1}	$K_{\rm bol}$
1	0.191 ± 0.027	554.55 ± 76.63	105.98 ± 1.48	4.82
2	0.113 ± 0.018	2.65 ± 0.43	0.30 ± 0.01	9.8
3	0.159 ± 0.022	96.37 ± 13.32	15.34 ± 0.14	7.41
4	0.237 ± 0.071	82.02 ± 24.56	19.45 ± 0.17	6.98
5	0.086 ± 0.024	110.65 ± 30.58	9.51 ± 0.09	7.26
6	0.269 ± 0.037	59.42 ± 8.21	16.00 ± 0.17	7.11
7	0.128 ± 0.030	73.10 ± 16.84	9.38 ± 0.09	7.21
8	0.119 ± 0.002	25.94	3.09 ± 0.05	8.18
9	0.051 ± 0.011	236.56 ± 49.03	12.06 ± 0.13	7.22
10	0.202 ± 0.186	32.65 ± 30.08	6.59 ± 0.09	7.56
11	0.129 ± 0.024	0.71 ± 0.13	0.09 ± 0.01	10.54
12	0.249 ± 0.344	16.37 ± 22.61	4.07 ± 0.06	7.95
13	0.049 ± 0.015	103.26 ± 30.92	5.01 ± 0.06	7.79
14	0.358 ± 0.058	39.26 ± 6.33	14.04 ± 0.17	6.91
15	0.127 ± 0.024	8.02 ± 1.48	1.02 ± 0.02	9.02
16	0.183 ± 0.080	6.08 ± 2.66	1.11 ± 0.03	9.03
17	0.078 ± 0.001	13	1.01 ± 0.02	9.05
18	0.170 ± 0.003	13	2.21 ± 0.04	8.47
19	0.183 ± 0.038	7.48 ± 1.55	1.37 ± 0.03	8.9
20	0.159 ± 0.026	14.25 ± 2.30	2.27 ± 0.04	8.42
28	0.166 ± 0.003	13	2.15 ± 0.04	8.25
33	0.243 ± 0.101	2.53 ± 1.05	0.61 ± 0.02	9.24
36	0.107 ± 0.054	23.12 ± 11.71	2.47 ± 0.07	8.15

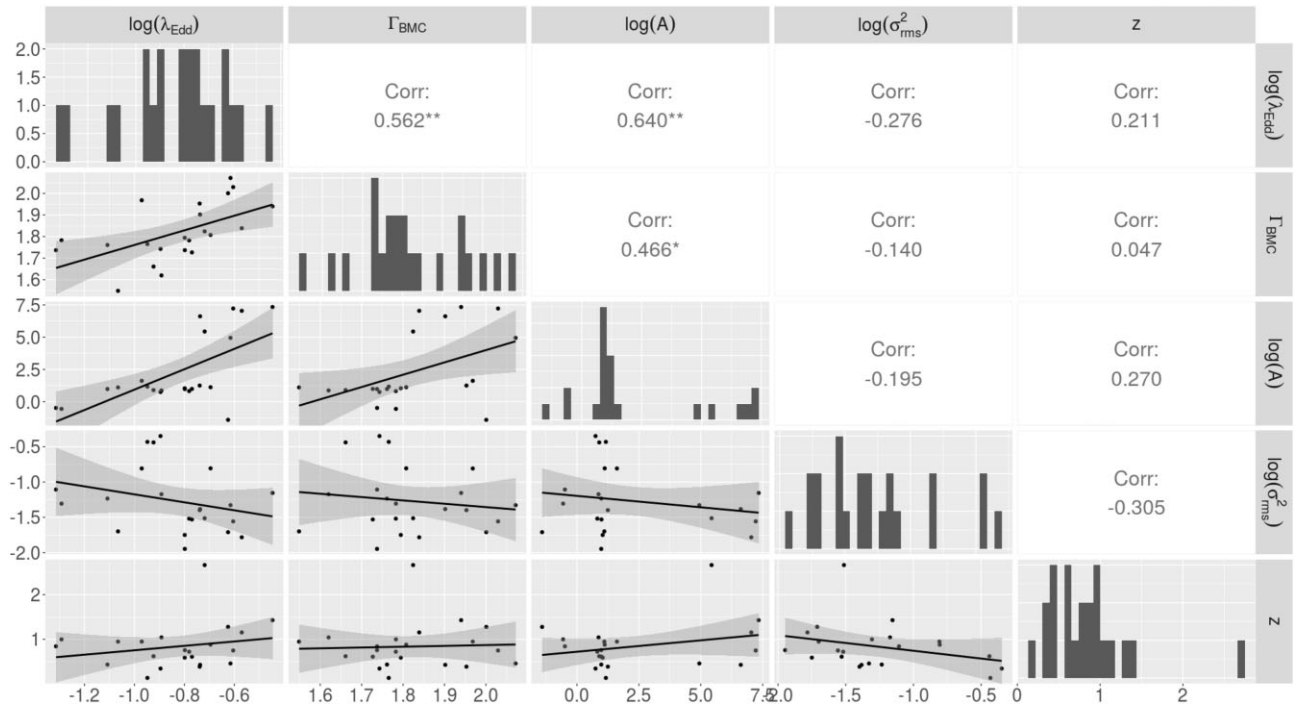

Figure 13. Correlogram of the main parameters of our AGNs including λ_{Edd}. Upper panels: Spearman rank coefficient between each pair of variables. Diagonal: individual histograms. Lower panels: scatter plots with regression lines and confidence intervals. The '∗' and '∗∗' symbols represent a moderate and strong correlation, respectively.

Downloaded from https://academic.oup.com/mnras/article/532/2/1564/7706312 by Instituto Nac. de Astrofisica, optica y Electronica (INAOE) user on 11 July 2024

Table 5. Summary of the main correlations.

Equation	Variables	Formula	S	p_{value}
4	$EW_{\rm Fe}$, Lx	$\log\left(\frac{EW_{Fe}}{keV}\right)_{det} = (-1.10 \pm 0.06) + (-0.23 \pm 0.07)\log\left(\frac{Lx}{10^{44}{\rm erg\,s^{-1}}}\right)$	-0.6	0.04
5	N_H, z	$\log(N_H) = (20.66 \pm 0.16) + (0.31 \pm 0.23)z$	0.45	> 0.05
13	$\sigma^2_{\rm rms}$, $M_{{\rm BH},X}$	$\log(\sigma^2_{\rm rms}) = (-1.46 \pm 0.05) + (-0.26 \pm 0.05)\log\left(\frac{M_{{\rm BH},X}}{10^8\,{\rm M}_\odot}\right)$	-0.26	≈ 0.05
14	$\sigma^2_{\rm rms}$, $L_{2-10\,{\rm keV}}$	$\log(\sigma^2_{\rm rms}) = (-1.37 \pm 0.04) + (-0.31 \pm 0.04)\log\left(\frac{L_{2-10\,{\rm keV}}}{10^{44}\,{\rm erg\,s^{-1}}}\right)$	-0.4	0.07
15	$L_{\rm bol}$, $M_{\rm BH}$, z	$\log\left(\frac{L_{bol}}{10^{44}\,erg\,s^{-1}}\right) = (0.39 \pm 0.19) + (0.75 \pm 0.17)\log\left(\frac{M_{BH}}{10^8\,{\rm M}_\odot}\right) + (0.57 \pm 0.10)z$	–	$\ll 0.05$
16	$\Gamma_{\rm BMC}$, $\lambda_{\rm Edd}$	$\Gamma_{BMC} = (2.10 \pm 0.09) + (0.34 \pm 0.11)\log(\lambda_{Edd})$	0.64	0.0014
18	$\lambda_{\rm Edd}$, $\log(A)$, $\Gamma_{\rm BMC}$	$\log(\lambda_{Edd}) = (0.18 \pm 0.05)\log(A) + (0.11 + 0.28)\Gamma_{BMC}$ $-(0.016 + 0.007)\log(A)^2 - (1.28 \pm 0.49)$	–	10^{-4}

2 detected in the XBS Survey, peaks at an Eddington ratio of 0.1, ranging from 0.001 to 0.5. Similarly, Nobuta et al. (2012) analysed 215 broad-line AGNs detected in the Subaru *XMM–Newton* field, with a mean redshift of $z \sim 1.4$. Their sample presents a λ_{Edd} lognormal distribution with a mean and standard deviation of 0.14 ± 0.2. Additionally, our bolometric correction factors are consistent with the $K_{\rm bol}$ confidence region reported by Duras et al. (2020).

6.1 $\lambda_{\rm Edd}$ versus other parameters

We study the relationship among the Eddington ratio and other physical parameters, including $\sigma^2_{\rm rms}$, z, the hard X-ray photon index $\Gamma_{\rm BMC}$, and the illumination factor $\log(A)$. We performed a multilinear regression analysis among those parameters, resulting in the correlation matrix presented in Fig. 13. This correlogram is composed of scatter plots with regression lines and confidence intervals (lower-panels), histograms (diagonal), and the results with a 95 per cent of confidence level of the Spearman rank coefficient between each pair of variables (upper panels). To maintain consistency with the previous linear regression analysis computed in Section 4, we did not consider the source with the lowest mass for the correlogram.

We found a strong and significant correlations between $\lambda_{\rm Edd} - \Gamma_{\rm BMC}$ ($S = 0.64$, $p_{\rm value} = 0.0014$) and $\lambda_{\rm Edd} - \log(A)$ ($S = 0.56$, $p_{\rm value} = 0.0037$). The relation between those physical properties weighted by the illumination factor is presented in Fig. 14 (upper). The simple linear regression equation for $\lambda_{\rm Edd} - \Gamma$ is expressed as follows:

$$\Gamma_{\rm BMC} = (2.10 \pm 0.09) + (0.34 \pm 0.11)\log(\lambda_{\rm Edd}) \quad (16)$$

By including the illumination factor in a third axis, we obtained a 3D plot presented in Fig. 14 (lower). The projected plane that best fits our data is calculated with equation (17). We obtained a significant relationship with $p_{\rm value} = 3.265 \times 10^{-5}$, which indicates a strong correlation between these three components. We mark with a black circle the source XID-4, which is the only source that did not follow the $\log(\lambda_{\rm Edd}) - \Gamma - \log(A)$ plane:

$$\log(A) = (3.4 \pm 3.2)\Gamma_{\rm BMC} + (30.9 + 10.7)\log(\lambda_{\rm Edd}) + (12.8 + 5.7)\log(\lambda^2_{\rm Edd}) + (12.6 \pm 9.1). \quad (17)$$

A similar relation is computed in equation (18) to estimate the Eddington ratio as a function of $\Gamma_{\rm BMC}$ and $\log(A)$. Finally, we did not find a clear relation among $\lambda_{\rm Edd}$ and other properties, for instance, the Normal Excess Variance and the redshift.

$$\log(\lambda_{\rm Edd}) = (0.18 \pm 0.05)\log(A) + (0.11 + 0.28)\Gamma_{\rm BMC} - (0.016 + 0.007)\log(A)^2 - (1.28 \pm 0.49). \quad (18)$$

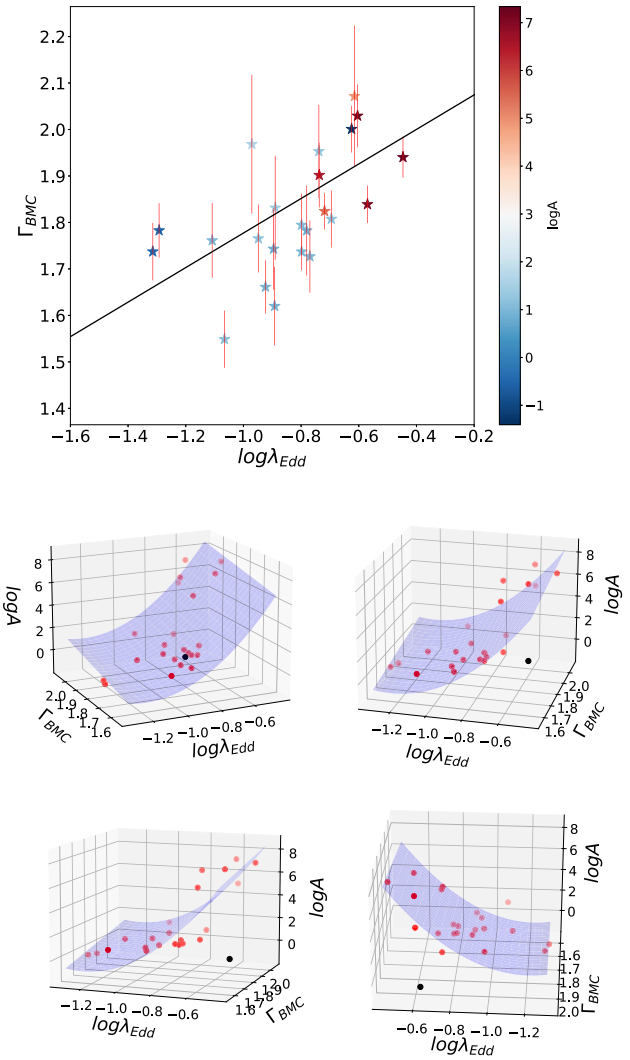

Figure 14. $\Gamma_{\rm BMC}$, $\lambda_{\rm Edd}$, and $\log(A)$ distribution of our AGN sample. Upper: 2D view. Lower: 3D view. The black line and the central plane represent the best regression fit of our data.

We should be cautious with the interpretation of these results, primarily because the method used to estimate $M_{\rm BH}$ and, consequently, λ_{Edd} may introduce bias. On the other hand, this multiple correlation may arise naturally from the connection between the accretion flow and the hot corona. For instance, previous studies have confirmed a strong correlation between the Eddington ratio and the

Downloaded from https://academic.oup.com/mnras/article/532/2/1564/7706312 by Instituto Nac. de Astrofisica, optica y Electronica (INAOE) user on 11 July 2024

X-ray photon index (e.g. Brightman et al. 2013; Sarma et al. 2015), suggesting that the accretion rate represented by λ_{Edd} could drive the physical conditions of the hot corona and the accretion disc. In this scenario, higher Eddington ratios are equivalent to higher accretion rates that can lead to a more efficient release of energy near the black hole. This excess energy can result in the production of higher-energy X-ray photons through Comptonization by the hot corona. Furthermore, as AGNs evolve, their accretion rates, the coverage of the hot corona over the effective disk area, and the spectral properties could change, therefore, the $\log(\lambda_{\rm Edd}) - \Gamma - \log(A)$ plane could be used to understand the transitional phases in AGN evolution, such as the transition from a high accretion rate Seyfert (NLSy1) to a normal Seyfert.

7 SUMMARY AND CONCLUSIONS

Since X-ray emission is an intrinsic property observed in all AGNs, X-ray analysis of multi-epoch observations of AGNs is a powerful tool to identify and study AGNs. In this paper, we performed a multi-epoch X-ray spectral analysis on a bright AGN sample with the highest S/N observed in the XMM−UNDF, which is one of the deepest X-ray surveys carried out with the satellite *XMM–Newton*. A summary of the main correlations presented in this paper is provided in Table 5. The key results of this analysis are listed below.

(i) The best model that fits our data is a combination of a simple power-law with a constant Galactic absorption, a neutral intrinsic absorption associated with the host galaxy, and a Fe−Kα emission line. We found a mean and standard deviation for the column density and the Fe−Kα line equivalent width of $\log(N_{\rm H}) = 20.92 \pm 0.18\,{\rm cm}^{-2}$ and ${\rm EW}_{\rm Fe} = 0.14 \pm 0.11$ keV, respectively.

(ii) We found statistically significant anticorrelation between the X-ray luminosity and the Fe−Kα equivalent width of our AGN sample, which is consistent with the 'Iwasawa−Taniguchi effect' associated with the decreasing of the torus opening angle as a function of L_x. It can be well described by ${\rm EW}_{\rm Fe} \propto L_{2-10\,{\rm keV}}^{-0.23}$.

(iii) For the relation between $N_{\rm H}$ and z, we found a moderate correlation consistent with the reported by Iwasawa et al. (2020) with the XMM deep survey in the CDFS and Corral et al. (2011) with the XBS. Our results suggest a potential trend in the evolution of the obscured AGN fraction towards higher redshifts.

(iv) We obtained a good agreement between the two approaches used to estimate the BH masses. For the X-ray luminosity method, the mean black hole mass was estimated to be $\log(M_{{\rm BH},L_x}/{\rm M}_\odot) = 7.59 \pm 0.59$, while the X-ray scaling method yielded a mean black hole mass of $\log(M_{{\rm BH},X}/{\rm M}_\odot) = 7.26 \pm 0.68$. We found a trend of slightly lower masses obtained with the luminosity method, described as $M_{{\rm BH},L_x} \sim 0.33 \times M_{{\rm BH},X}$.

(v) The $L_x - \sigma^2_{\rm rms}$ and the $M_{\rm BH} - \sigma^2_{\rm rms}$ distributions present statistically significant anti-correlations with roughly the same flat slopes with $m = -0.31 \pm 0.4$ and $m = -0.26 \pm 0.05$, respectively. These results support the possibility that the anti-correlation between the luminosity and X-ray variability arises as a consequence of an intrinsic relationship between the BH mass and the X-ray variability.

(vi) Our AGN sample covers the bolometric luminosity range of $42.5 < \log(L_{\rm bol}) < 46.1$ with moderate dispersion in the Eddington ratio distribution, with a mean of $\lambda_{\rm Edd} = 0.16 \pm 0.07$. Additionally, our analysis reveals strong correlations between $\Gamma_{\rm BMC}$, $\lambda_{\rm Edd}$, and $\log(A)$. Studying this parameter space could offer a novel perspective on the changing stages of AGN evolution.

ACKNOWLEDGEMENTS

MEC acknowledges support from Consejo Nacional de Humanidades, Ciencias y Tecnologías (CONAHCYT) through a postdoctoral fellowship within the program 'Estancias Posdoctorales por México'. ALL acknowledges support from CONAHCYT grant CB-2016-286316 and Programa de Apoyo a Proyectos de Investigación e Innovación Tecnológica (PAPIIT) IA-101623. T. Miyaji is supported by UNAM Dirección General de Asuntos del Personal Académico (DGAPA) PAPIIT 114423. YK acknowledges support from DGAPA-PAPIIT grant IN102023.

DATA AVAILABILITY

The data underlying this article will be shared on reasonable request to the corresponding author.

REFERENCES

Akaike H., 1974, IEEE Trans. Automatic Control, 19, 716
Beuchert T. et al., 2015, A&A, 584, A82
Bianchi S., Guainazzi M., Matt G., Fonseca Bonilla N., 2007, A&A, 467, L19
Brandt W. N., Alexander D. M., 2015, A&AR, 23, 1
Brandt W. N., Vito F., 2017, Astron. Nachr., 338, 241
Brightman M. et al., 2013, MNRAS, 433, 2485
Burlon D., Ajello M., Greiner J., Comastri A., Merloni A., Gehrels N., 2011, ApJ, 728, 58
Caccianiga A., Fanali R., Severgnini P., Della Ceca R., Marchese E., Mateos S., 2013, A&A, 549, A119
Chen C. T. J., Brandt W. N., Luo B., Ranalli P., Yang G., Alexander D. M., Bauer F. E., Kelson D. D., 2018, MNRAS, 478, 2132
Corral A., Della Ceca R., Caccianiga A., Severgnini P., Brunner H., Carrera F. J., Page M. J., Schwope A. D., 2011, A&A, 530, A42
Cutri R. M. et al., 2021, VizieR Online Data Catalog, p. II/328
D'Amato Q. et al., 2020, A&A, 636, A37
Della Ceca R. et al., 2004, A&A, 428, 383
Duras F. et al., 2020, A&A, 636, A73
Elías-Chávez M., Longinotti A. L., Krongold Y., Vignali C., Nicastro F., Rosa-González D., Mayya Y. D., Mathur S., 2021, ApJ, 919, 18
Fabian A. C., Vasudevan R. V., Gandhi P., 2008, MNRAS, 385, L43
Farinelli R., Titarchuk L., Paizis A., Frontera F., 2008, ApJ, 680, 602
Fragile P. C., Miller W. A., Vandernoot E., 2005, ApJ, 635, 157
Gabriel C. et al., 2004, in Ochsenbein F., Allen M. G., Egret D., eds, Astronomical Society of the Pacific Conference Series Vol. 314, Astronomical Data Analysis Software and Systems (ADASS) XIII. Astronomical Society of the Pac., San Francisco, p. 759
Georgakakis A., Aird J., Schulze A., Dwelly T., Salvato M., Nandra K., Merloni A., Schneider D. P., 2017, MNRAS, 471, 1976
George I. M., Fabian A. C., 1991, MNRAS, 249, 352
Gilli R., Comastri A., Hasinger G., 2007, A&A, 463, 79
Gilli R. et al., 2022, A&A, 666, A17
Gliozzi M., Titarchuk L., Satyapal S., Price D., Jang I., 2011, ApJ, 735, 16
Gliozzi M., Williams J. K., Michel D. A., 2021, MNRAS, 502, 3329
Haardt F., Maraschi L., 1991, ApJ, 380, L51
Hebbar P. R., Heinke C. O., Sivakoff G. R., Shaw A. W., 2019, MNRAS, 485, 5604
Hickox R. C., Alexander D. M., 2018, ARA&A, 56, 625
Iwasawa K., Taniguchi Y., 1993, ApJ, 413, L15
Iwasawa K. et al., 2020, A&A, 639, A51
Kellermann K. I., Fomalont E. B., Mainieri V., Padovani P., Rosati P., Shaver P., Tozzi P., Miller N., 2008, ApJS, 179, 71
Kormendy J., Richstone D., 1995, ARA&A, 33, 581
Krongold Y. et al., 2021, ApJ, 917, 39
Lanzuisi G. et al., 2014, ApJ, 781, 105
Laurenti M. et al., 2022, A&A, 657, A57

Downloaded from https://academic.oup.com/mnras/article/532/2/1564/7706312 by Instituto Nac. de Astrofisica, optica y Electronica (INAOE) user on 11 July 2024

Liu T. et al., 2017, ApJS, 232, 8
Liu T. et al., 2022, A&A, 661, A5
Luo B. et al., 2017, ApJS, 228, 2
Mateos S. et al., 2008, A&A, 492, 51
Mateos S. et al., 2010, A&A, 510, A35
Mathur S., Kuraszkiewicz J., Czerny B., 2001, New Astron., 6, 321
Matt G. et al., 1997, A&A, 325, L13
McHardy I. M., Papadakis I. E., Uttley P., Page M. J., Mason K. O., 2004, MNRAS, 348, 783
Netzer H. , (ed.), 2013, The Physics and Evolution of Active Galactic Nuclei, Cambridge University Press, Cambridge, UK, p. 157
Netzer H., 2019, MNRAS, 488, 5185
Nicastro F. et al., 2018, Nature, 558, 406
Nikolajuk M., Papadakis I. E., Czerny B., 2004, MNRAS, 350, L26
Nobuta K. et al., 2012, ApJ, 761, 143
Papadakis I. E., Chatzopoulos E., Athanasiadis D., Markowitz A., Georgantopoulos I., 2008, A&A, 487, 475
Peterson B. M. et al., 2004, ApJ, 613, 682
Ponti G., Papadakis I., Bianchi S., Guainazzi M., Matt G., Uttley P., Bonilla N. F., 2012, A&A, 542, A83
Rees M. J., 1978, Phys. Scr, 17, 193
Ricci C., Trakhtenbrot B., 2023, Nature Astronomy 7 1282
Ricci C., Ueda Y., Paltani S., Ichikawa K., Gandhi P., Awaki H., 2014, MNRAS, 441, 3622
Rosen S. R. et al., 2016, A&A, 590, A1
Sarma R., Tripathi S., Misra R., Dewangan G., Pathak A., Sarma J. K., 2015, MNRAS, 448, 1541
Scoville N. et al., 2007, ApJS, 172, 1
Shaposhnikov N., Titarchuk L., 2009, ApJ, 699, 453
Shrader C. R., Titarchuk L., 2003, ApJ, 598, 168
Shu X. W., Yaqoob T., Wang J. X., 2010, ApJS, 187, 581
Traulsen I. et al., 2019, A&A, 624, A77
Traulsen I. et al., 2020, A&A, 641, A137
Trump J. R. et al., 2011, ApJ, 733, 60
Uttley P., Casella P., 2014, Space Sci. Rev., 183, 453
Williams J. K., Gliozzi M., Bockwoldt K. A., Shuvo O. I., 2023, MNRAS, 521, 2897
Wilms J., Allen A., McCray R., 2000, ApJ, 542, 914
Xue Y. Q. et al., 2011, ApJS, 195, 10
Yang G. et al., 2016, ApJ, 831, 145
Yuan F., Narayan R., 2014, ARA&A, 52, 529
Zheng X. C. et al., 2017, ApJ, 849, 127
Zwillinger D., Kokoska S., 2000, Zwillinger Daniel CRC standard probability and statistics tables and formulae. Chapman and Hall/CRC, Boca Raton, Florida, USA 373

APPENDIX A: AGN SAMPLE SPECTRA

*XMM–Newton*0.3–10 keV rest-frame spectra of our sample composed of 23 AGNs detected in the XMM–UNDF with mean X-ray photon counts of 10 000 cts. Each spectrum is composed by the combination of the 3 cameras with the 11 observations, as was explained in Section 3. The data were modelled with their best fit according to table 2, i.e. a combination of a simple power-law, constant Galactic absorption of $N_{\rm H} = 3.56 \times 10^{20}\,{\rm cm}^{-2}$, and an iron emission line at 6.4 keV. While the residuals are presented in terms of the data minus the model weighted by the error.

y-axis in the upper panel in all plots is in terms of 'normalized counts $s^{-1}\,keV^{-1}\,cm^{-2}$', while the *y*-axis in the lower panel in all plots is in terms of '(data–model)/error'.

Downloaded from https://academic.oup.com/mnras/article/532/2/1564/7706312 by Instituto Nac. de Astrofisica, optica y Electronica (INAOE) user on 11 July 2024

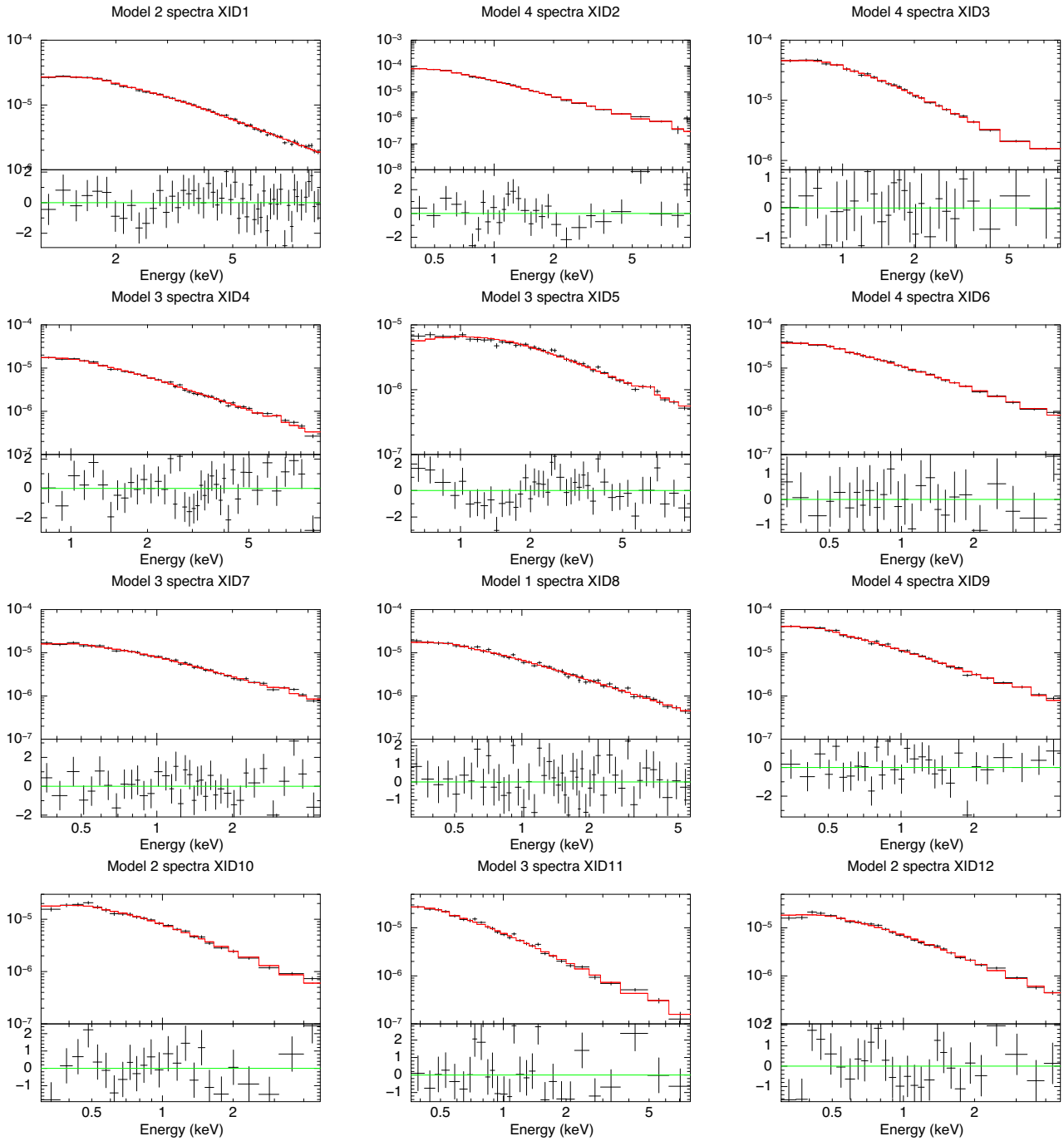

Figure A1. Spectra of the AGN sample and their residuals part-1.

Downloaded from https://academic.oup.com/mnras/article/532/2/1564/7706312 by Instituto Nac. de Astrofisica, optica y Electronica (INAOE) user on 11 July 2024

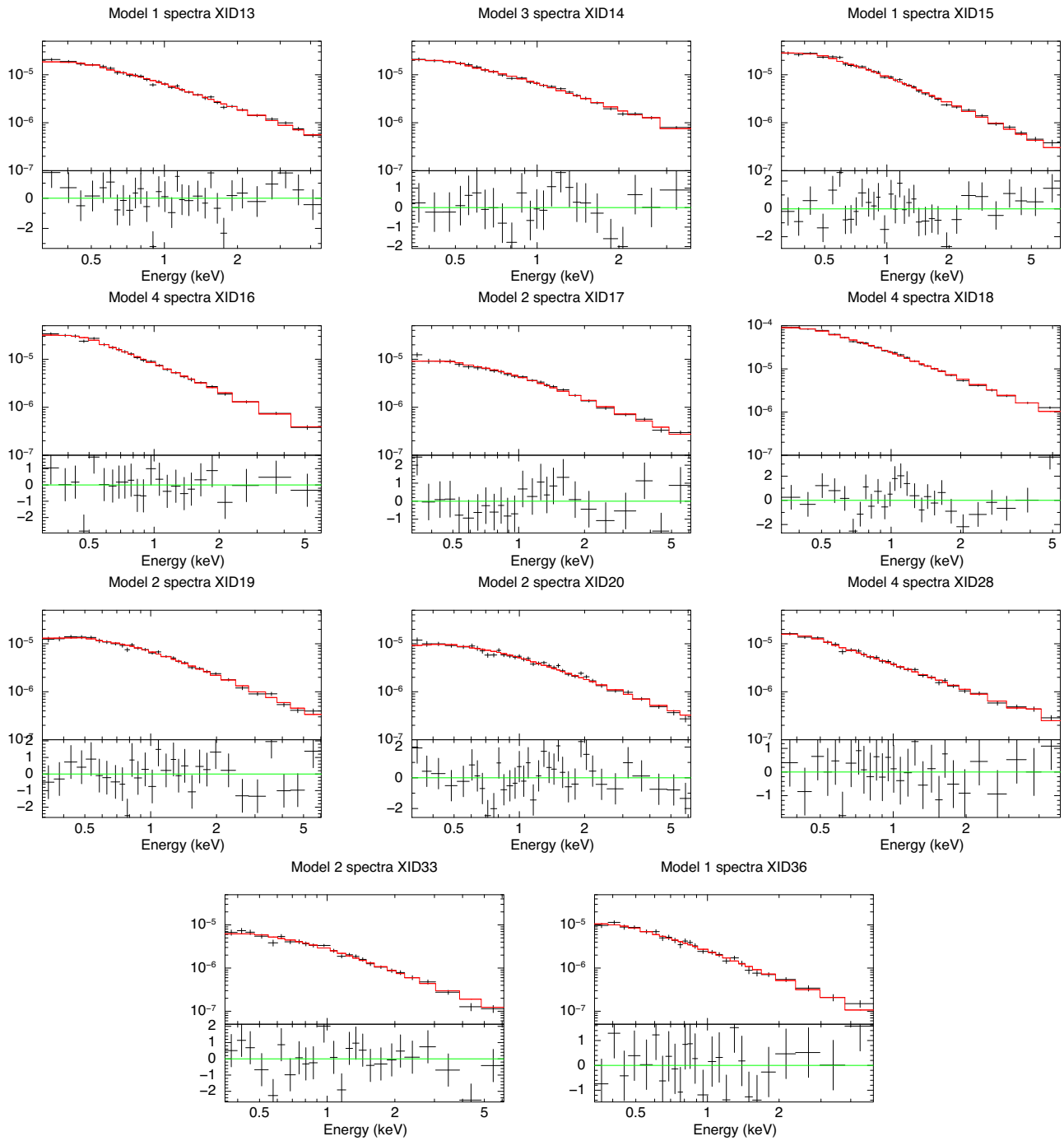

Figure A2. Spectra of the AGN sample and their residuals part-2.

This paper has been typeset from a TEX/LATEX file prepared by the author.

Downloaded from https://academic.oup.com/mnras/article/532/2/1564/7706312 by Instituto Nac. de Astrofisica, optica y Electronica (INAOE) user on 11 July 2024

© 2024 The Author(s).
Published by Oxford University Press on behalf of Royal Astronomical Society. This is an Open Access article distributed under the terms of the Creative Commons Attribution License (https://creativecommons.org/licenses/by/4.0/), which permits unrestricted reuse, distribution, and reproduction in any medium, provided the original work is properly cited.